

# Participant and spectator scaling of spectator fragments in Au+Au and Cu+Cu collisions at $\sqrt{s_{NN}} = 19.6$ and $22.4$ GeV.

B.Alver<sup>4</sup>, B.B.Back<sup>1</sup>, M.D.Baker<sup>2</sup>, M.Ballintijn<sup>4</sup>, D.S.Barton<sup>2</sup>, R.R.Betts<sup>6</sup>, A.A.Bickley<sup>7</sup>, R.Bindel<sup>7</sup>, A.Budzanowski<sup>3</sup>, W.Busza<sup>4</sup>, A.Carroll<sup>2</sup>, Z.Chai<sup>2</sup>, V.Chetluru<sup>6</sup>, M.P.Decowski<sup>4</sup>, E.García<sup>6</sup>, T.Gburek<sup>3</sup>, N.George<sup>1,2</sup>, K.Gulbrandsen<sup>4</sup>, S.Gushue<sup>2</sup>, C.Halliwell<sup>6</sup>, J.Hamblen<sup>8</sup>, I.Harnarine<sup>6</sup>, G.A.Heintzelman<sup>2</sup>, C.Henderson<sup>4</sup>, D.J.Hofman<sup>6</sup>, R.S.Hollis<sup>6</sup>, R.Holyński<sup>3</sup>, B.Holzman<sup>2</sup>, A.Iordanova<sup>6</sup>, E.Johnson<sup>8</sup>, J.L.Kane<sup>4</sup>, J.Katzy<sup>4,6</sup>, N.Khan<sup>8</sup>, W.Kucewicz<sup>6</sup>, P.Kulinich<sup>4</sup>, C.M.Kuo<sup>5</sup>, W.Li<sup>4</sup>, W.T.Lin<sup>5</sup>, C.Loizides<sup>4</sup>, S.Manly<sup>8</sup>, D.McLeod<sup>6</sup>, A.C.Mignerey<sup>7</sup>, R.Nouicer<sup>6</sup>, A.Olszewski<sup>3</sup>, R.Pak<sup>2</sup>, I.C.Park<sup>8</sup>, H.Pernegger<sup>4</sup>, C.Reed<sup>4</sup>, L.P.Remsberg<sup>2</sup>, M.Reuter<sup>6</sup>, E.Richardson<sup>7</sup>, C.Roland<sup>4</sup>, G.Roland<sup>4</sup>, L.Rosenberg<sup>4</sup>, J.Sagerer<sup>6</sup>, P.Sarin<sup>4</sup>, P.Sawicki<sup>3</sup>, I.Sedykh<sup>2</sup>, W.Skulski<sup>8</sup>, C.E.Smith<sup>6</sup>, M.A.Stankiewicz<sup>2</sup>, P.Steinberg<sup>2</sup>, G.S.F.Stephans<sup>4</sup>, A.Sukhanov<sup>2</sup>, A.Szostak<sup>2</sup>, J.-L.Tang<sup>5</sup>, M.B.Tonjes<sup>7</sup>, A.Trzupek<sup>3</sup>, C.Vale<sup>4</sup>, G.J.van Nieuwenhuizen<sup>4</sup>, S.S.Vaurynovich<sup>4</sup>, R.Verdier<sup>4</sup>, G.I.Verés<sup>4</sup>, P.Walters<sup>8</sup>, E.Wenger<sup>4</sup>, D.Willhelm<sup>7</sup>, F.L.H.Wolfs<sup>8</sup>, B.Wosiek<sup>3</sup>, K.Woźniak<sup>3</sup>, A.H.Wuosmaa<sup>1</sup>, S.Wyngaardt<sup>2</sup>, B.Wysłouch<sup>4</sup>

<sup>1</sup> Physics Division, Argonne National Laboratory, Argonne, IL 60439-4843, USA

<sup>2</sup> Brookhaven National Laboratory, Upton, NY 11973-5000, USA

<sup>3</sup> Institute of Nuclear Physics, Kraków, Poland

<sup>4</sup> Laboratory for Nuclear Science, Massachusetts Institute of Technology, Cambridge, MA 02139-4307, USA

<sup>5</sup> Department of Physics, National Central University, Chung-Li, Taiwan

<sup>6</sup> Department of Physics, University of Illinois at Chicago, Chicago, IL 60607-7059, USA

<sup>7</sup> Department of Chemistry, University of Maryland, College Park, MD 20742, USA

<sup>8</sup> Department of Physics and Astronomy, University of Rochester, Rochester, NY 14627, USA

(Dated: November 7, 2015)

Spectator fragments resulting from relativistic heavy ion collisions, consisting of single protons and neutrons along with groups of stable nuclear fragments up to Nitrogen ( $Z = 7$ ), are measured in PHOBOS. These fragments are observed in Au+Au ( $\sqrt{s_{NN}} = 19.6$  GeV) and Cu+Cu (22.4 GeV) collisions at high pseudorapidity ( $\eta$ ). The dominant multiply-charged fragment is the tightly bound Helium ( $\alpha$ ), with Lithium, Beryllium, and Boron all clearly seen as a function of collision centrality and pseudorapidity. We observe that in Cu+Cu collisions, it becomes much more favorable for the  $\alpha$  fragments to be released than Lithium. The yields of fragments approximately scale with the number of spectator nucleons, independent of the colliding ion. The shapes of the pseudorapidity distributions of fragments indicate that the average deflection of the fragments away from the beam direction increases for more central collisions. A detailed comparison of the shapes for  $\alpha$  and Lithium fragments indicates that the centrality dependence of the deflections favors a scaling with the number of participants in the collision.

## I. INTRODUCTION

In relativistic heavy ion collisions, the nucleons of the interacting ions can be divided into two distinct categories: those that experience an inelastic collision with at least one nucleon from the opposing nucleus (participants) and those that do not (spectators). Participant nucleons ultimately create the bulk of particles observed in the detectors. Spectators consist of single protons and neutrons as well as larger spectator fragments including Helium, Lithium, Beryllium, Boron, and higher mass nuclei. Naïvely, these spectators are free to continue along their original path as they do not directly participate in the collision. In practice, however, they can interact in several ways and still be considered a spectator by the usual definition: for example they can suffer an elastic collision with a nucleon from the other beam, they can be affected by any remaining nuclear binding energy in the beam remnant, or they can interact with produced particles from the participant zone [1].

Fragmentation of nuclei has been studied in a number of experiments [2–9]. These experiments typically

covered the full kinematic and solid angle range needed to accurately identify all fragments and basic fragment properties such as  $A$  and  $Z$ , and their momenta. However, these experiments suffer from a lack of statistics, with only  $\mathcal{O}(1000)$  events in total, precluding detailed differential studies of fragmentation properties as a function of impact parameter.

The observed properties of fragments, such as their momentum vectors, can be described by a combination of the beam momentum at the time of the collision and the internal Fermi motion within the nucleus in its rest frame. In the absence of Fermi motion and other external effects, spectator fragment transverse momenta would be zero and they would consequently continue traveling at the same rapidity as the beam. In this limit, the polar angle ( $\theta$ ) of fragments would be zero or, equivalently, they would have infinite pseudorapidity ( $\eta$ ):

$$\begin{aligned} \eta &= -\ln(\tan(\theta/2)) \\ &\rightarrow \infty(\theta \rightarrow 0). \end{aligned} \quad (1)$$

Including the Fermi motion, however, leads to a finite

transverse momentum component of the fragments and reduces the particle rapidity to below that of the beam. With a finite (nonzero) polar angle, it is possible that the products will be intercepted by active elements of a detector. In addition, the internal Fermi motion also modifies the longitudinal component of the momentum, however this effect is typically small compared to the boosted momentum of the nucleons.

Transverse momentum is boost invariant and it therefore becomes useful to compare data across multiple experiments with differing collision energies. Equivalently, by converting the momentum vectors into an angular form, one can show that the pseudorapidity density distribution ( $dN/d\eta$  versus  $\eta$ ) becomes approximately boost invariant, which also allows for the comparison of data at different  $\sqrt{s_{NN}}$ . To account for energy differences, one subtracts the rapidity of the beam at the appropriate energy scale; a nontrivial transformation described in Appendix A.

In the PHOBOS experiment [10] at the Relativistic Heavy-Ion Collider (RHIC), completely-freed neutrons can be measured using the Zero-Degree Calorimeters (ZDC) [11], which are specifically designed for this purpose. Charged fragments are not observed in these detectors as they are swept away from the ZDCs by the RHIC accelerator magnets. A calorimeter that could detect very forward protons was later added to the PHOBOS setup, but was not available for this analysis. At RHIC injection energies, nucleon-nucleon center of mass energy  $\sqrt{s_{NN}} = 19.6$  (Au+Au) and 22.4 GeV (Cu+Cu), spectators with a finite transverse momentum can be detected within the pseudorapidity acceptance of PHOBOS. However, the finite acceptance of the detector limits the measurement of very low- $p_T$  particles, especially for large- $Z$  fragments. A large statistical sample, though, has been amassed which does allow for some more detailed studies not afforded to other experiments.

This paper presents detailed measurements of large- $Z$  fragments in the PHOBOS detector. Section II describes the detector. Section III describes the analysis methods used to distinguish differently charge particles. Sections IV and V show the pseudorapidity and centrality dependencies of the fragments, respectively. Section V B discusses how, in combining the system size, centrality, and pseudorapidity dependencies, one can probe scaling effects of the large- $Z$  fragments in the context of the number of spectators and participants in the collision.

## II. PHOBOS DETECTOR

PHOBOS is a large acceptance silicon detector, covering almost  $2\pi$  in azimuth and  $|\eta| < 5.4$  ( $\theta > 9$  mrad) [10]. For the results presented here, the energy loss measured in the Ring detectors ( $3.0 < |\eta| < 5.4$ ) is used to identify spectator fragments. The Rings are silicon pad detectors arranged in an octagonal pattern perpendicular to and surrounding the beam pipe. Three Ring detectors

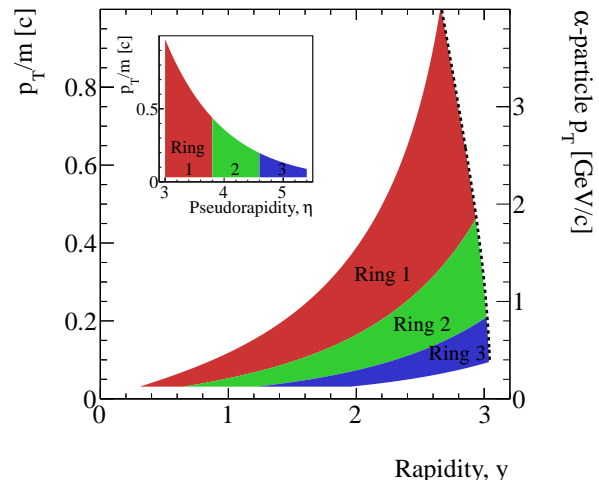


FIG. 1. (color online) Transverse momentum and rapidity coverage of charged particles in the silicon Ring detectors in PHOBOS. The main figure shows the  $p_T/m$ -rapidity acceptance for charged particles in each Ring (different shaded bands). The boundary on the rightmost edge of the shaded region depends on the beam energy. The dashed line shows the boundary for  $p_z/m = p_{\text{beam}}/m_{\text{Au}}$  for  $\sqrt{s_{NN}} = 19.6$  GeV Au+Au collisions. The right-hand axis shows the  $p_T$ -scale for  $\alpha$  particles, i.e.  $m = 3.727$  GeV/ $c^2$ . The inset figure shows the Ring-detector  $p_T$  and pseudorapidity coverage.

are placed on each side of the interaction point at approximately 1, 2, and 5 meters from the center of the interaction region. This configuration allows for full coverage with minimal overlapping areas. In addition, the Octagon silicon barrel, which consists of a single-layer of silicon parallel to and surrounding the beam pipe covering  $|\eta| < 3.2$ , is used for collision vertex and event centrality determination.

In order to distinguish between singly- and multiply-charged fragments, the relative energy loss,  $E_{\text{rel}}$ , is defined as

$$E_{\text{rel}} = \frac{E_{\text{loss}}}{\langle E_{\text{loss}} \rangle_{Z=1}}, \quad (2)$$

where  $E_{\text{loss}}$  is the energy loss in the silicon detector and  $\langle E_{\text{loss}} \rangle_{Z=1}$  is the mean energy loss for a  $Z = 1$  particle. Singly-charged particles (for example spectator protons, deuterons, and tritons) and singly-charged participants or produced particles (created by the participants) all appear at an  $E_{\text{rel}}$  position close to 1 and, as such, cannot be separated. For larger fragments, with charge greater than unity, energy loss in the silicon follows a charge-squared ( $Z^2$ ) dependence, leading to the appearance of  $\alpha$  particles (for example) at four times the  $E_{\text{rel}}$  position of a singly-charged particle.

The transverse momentum,  $p_T$ , and rapidity,  $y$ , coverage for charged particles in the Rings is shown in

140 Fig. 1. As there is no significant magnetic field traversed  
 141 by forward-going particles, the fixed  $\eta$  Ring boundaries  
 142 translate to fixed curves in  $p_T/m$  versus  $y$  for all charged  
 143 particles. The high- $p_T$  and  $y$  boundary (rightmost edge  
 144 for each Ring) is calculated for  $\sqrt{s_{NN}} = 19.6$  GeV Au+Au  
 145 collisions, assuming a maximum  $p_z/m = p_{\text{beam}}/m_{\text{Au}}$ ,  
 146 where  $p_z$  is the momentum of the particle (of mass  $m$ )  
 147 along the beam direction, and  $p_{\text{beam}}$  is the beam momen-  
 148 tum.

### 149 III. DATA ANALYSIS

#### 150 A. Event Selection

151 The data were recorded during the 2001  
 152 (Au+Au -  $\sqrt{s_{NN}} = 19.6$  GeV) and 2005 (Cu+Cu -  
 153  $\sqrt{s_{NN}} = 22.4$  GeV) RHIC runs. Readout of the silicon  
 154 was initiated by a minimally biased trigger for each  
 155 data set based on coinciding signals from two arrays  
 156 of 16 plastic scintillators ( $3.2 < |\eta| < 4.5$ ), the “Paddle”  
 157 trigger counters [12]. For Au+Au (Cu+Cu) collisions,  
 158 a minimum of 3 (1) scintillator hits were required  
 159 in each array to start readout. The collision vertex  
 160 position along the beam line ( $z$ ) was determined via a  
 161 probabilistic approach using hits in the Octagon silicon  
 162 barrel [13]. For Cu+Cu collisions at  $\sqrt{s_{NN}} = 22.4$  GeV,  
 163 a vertex requirement of  $|z| < 10$  cm from the nominal  
 164 vertex position was imposed; for Au+Au this was  
 165 relaxed to  $|z| < 20$  cm to maximize the statistics from the  
 166 single day-long run. A total of 84k (2.1M) events were  
 167 selected for this analysis out of 327k (15.7M) recorded,  
 168 respectively for Au+Au (Cu+Cu) collisions. Events are  
 169 dominantly rejected due to the vertex requirement. The  
 170 estimated trigger efficiency (coupled with the vertex  
 171 finding efficiency) for the Au+Au (Cu+Cu) data set is  
 172  $83.5 \pm 3\%$  ( $79 \pm 5\%$ ), determined using the same methods  
 173 as described in Ref. [14] with the data divided into  
 174 seven (six) centrality classes, each with 10% of the  
 175 total nuclear inelastic cross-section. The centrality  
 176 measure, EOct, is the summed energy loss in the silicon  
 177 of the centrally located Octagon barrel in the region  
 178  $|\eta| < 3.0$  [14]. The EOct parameter is defined in a  
 179 region smaller than the full acceptance of the Octagon  
 180 to limit any systematic effects of acceptance shifts  
 181 (due to the collision vertex position) and to reduce the  
 182 overlap with the Ring detector acceptance. The lowest  
 183 centrality cut-off is defined as the point at which the  
 184 trigger+vertex efficiency falls below 100%. For each  
 185 centrality class, the number of participants ( $N_{\text{part}}$ ) is  
 186 estimated by use of a Glauber model calculation [15].  
 187 Also, the number of spectator nucleons emitted at either  
 188 the positive or negative pseudorapidity is calculated as  
 189  $N_{\text{spec}}/2 = (N_{\text{part}}^{\text{max}} - N_{\text{part}})/2$ , where  $N_{\text{part}}^{\text{max}} = 2A = 394$  (126)  
 190 for Au (Cu) nuclei.

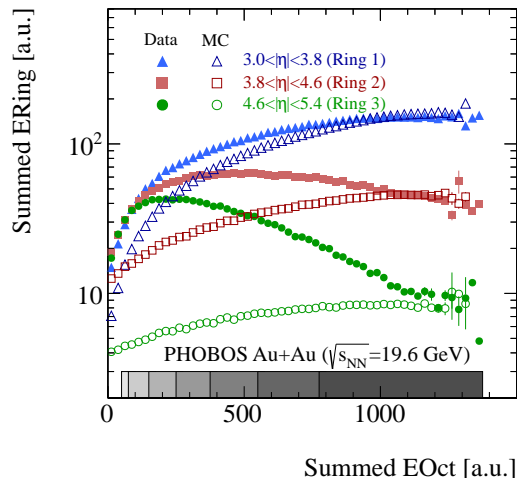


FIG. 2. (color online) Correlation between the summed energy recorded in each of the Ring detectors (ERing) and the summed energy deposited in the Octagon barrel (EOct) in Au+Au collisions at  $\sqrt{s_{NN}} = 19.6$  GeV. Filled (open) symbols illustrate the measured distributions from data (simulation). Spectators have been explicitly excluded from the simulation distributions. The bands show the centrality class selection bins used in this analysis, with darker bands corresponding to more central events. See text for discussion.

#### B. Motivation

The first hint of the presence of charged spectator fragments, in the acceptance of PHOBOS, was made during the first low-energy data [16]. The measured charged particle multiplicity was observed to be larger at high pseudorapidity in peripheral data than in central data, an opposite effect than was expected, and in contrast to the observed dependencies at mid-rapidity. Several tests were performed to confirm that the larger particle yield at high pseudorapidity likely originated from spectator fragments. Figure 2 shows the correlation between the summed energy in each silicon ring (ERing) and the summed energy deposited in the silicon Octagon barrel (EOct). Filled symbols represent data; open symbols show the result of a Monte-Carlo (MC) simulation that uses particles generated from a HIJING [17] event simulation passed through a full GEANT [18] description of the PHOBOS detector and has had spectator fragments explicitly removed from the acceptance of the detector.

In the MC simulation, a monotonic correlation is observed between ERing 1 and EOct, which becomes weaker for larger pseudorapidities. Even at the highest pseudorapidities, ERing 3 still increases with increasing EOct. In the data, the dependence of ERing 1 on EOct is similar in shape to that found in the MC simulation. At higher pseudorapidities, however, the positive correlation is restricted to the lowest EOct range and, after reaching a maximum, ERing 2 and ERing 3 start to decrease with

219 increasing EOct.

220 This same anticorrelated dependence was observed in 272  
 221 Au+Au data at higher energies in the correlation be-273  
 222 tween the Paddle Scintillator counters and the Zero De-274  
 223 gree Calorimeter (ZDCs). The ZDCs detect spectator 275  
 224 neutrons and include roughly the same relative  $\eta$  region 276  
 225 (i.e. when considering the difference in beam rapidi-277  
 226 ties ( $y_{\text{beam}}$ ) for different collision energies:  $\eta - y_{\text{beam}}$ ) in 278  
 227  $\sqrt{s_{NN}} = 200$  GeV collisions as covered by Rings 2 and 3 279  
 228 for 19.6 GeV, see for example Ref. [19]. It is possible that 280  
 229 the multiplicity distribution from produced particles nar-281  
 230 rows for more central collisions [20], however this could 282  
 231 not account for the observed rise/fall behavior. 283

### 232 C. Fragment Identification 285

233 Fragments are identified using their relative energy loss 288  
 234 ( $E_{\text{rel}}$ ) in the silicon (see Eq. 2). Figure 3 shows the 289  
 235  $E_{\text{rel}}$  distribution measured in the ERing acceptance for 290  
 236 Au+Au collisions at  $\sqrt{s_{NN}} = 19.6$  GeV, where no central-291  
 237 ity selection is made and only the region  $5.0 < |\eta| < 5.4$  is 292  
 238 shown in order to make the higher mass fragments more 293  
 239 pronounced. In Fig. 3, the data is shown as a blue spec-294  
 240 trum along with the distribution expected from singly-295  
 241 charged particles ( $Z = 1$ , red). The latter is considered to 296  
 242 be a “background” to the data and is determined from a 297  
 243 MC simulation without spectator fragments. This  $Z = 1$  298  
 244 contribution can be explicitly subtracted as it is entirely  
 245 due to singly-charged particles (mostly from the collision)  
 246 with a typical Landau-like distribution.

### 247 D. Subtracting Singly-Charged Particles

248 To determine the spectral shape of the  $Z = 1$  contribu-  
 249 tion, the energy loss signal for single particles is modeled  
 250 using a full GEANT Monte-Carlo (MC) simulation of the  
 251 PHOBOS apparatus. In data and simulation, it is ob-  
 252 served that multiple  $Z = 1$  particles can impinge on a sin-  
 253 gle silicon sensor, causing an ensemble distribution over  
 254 many events to exhibit peaks at  $E_{\text{rel}} \sim 2$  and 3 (note that  
 255 these additional peaks are not clearly visible in Fig. 3).  
 256 The peak at  $E_{\text{rel}} \sim 2$  (which occurs at a rate of about 8%  
 257 at the highest pseudorapidities) has to be accounted for  
 258 in the  $Z = 1$  subtraction. The third peak is suppressed  
 259 to a rate of 0.6% and is ignored in this analysis. As  
 260 this rate is dependent on the charged-particle multiplicity  
 261 in each detector, this fraction varies with both central-  
 262 ity and pseudorapidity, an effect observed in both data  
 263 and simulation. Importantly, data with a lesser contribu-  
 264 tion from a second charged-particle effectively steepens  
 265 the spectrum, changing the amount of subtracted back-  
 266 ground.

267 To account for the second peak in the spectrum, both  
 268 data and MC are divided into five pseudorapidity and  
 269 seven (six) centrality classes for the Au+Au (Cu+Cu)  
 270 analysis, respectively. As the MC distribution only re-

271 flects the relative contribution of 1 and 2 singly charged-  
 272 particles, each class produces a spectrum which has a  
 273 unique shape. To account for the contribution of a sec-  
 274 ond singly charged particle, each data class is systemat-  
 275 ically compared to all centrality/pseudorapidity classes  
 276 from the MC, i.e. 35 comparisons, therefore testing the  
 277 data against a large sample of simulated 2/1 hits-per-  
 278 sensor contributions. Each MC class is normalized to  
 279 the data at the first peak (close to  $E_{\text{rel}} = 1$  in Fig. 3).  
 280 The optimal background is chosen as the one with the  
 281 least  $\chi^2$  difference between data and MC  $E_{\text{rel}}$  spectra,  
 282 formed over a region around the expected second peak  
 283 position ( $1.5 < E_{\text{rel}} < 2.5$ ).

284 To systematically test the sensitivity of the one-to-  
 285 two hits contribution,  $Z = 1$  MC simulation samples with  
 286 different one-to-two hits ratios are used in the analy-  
 287 sis. A systematic uncertainty due to the  $\chi^2$  procedure  
 288 is assigned by considering two further  $Z = 1$  distribu-  
 289 tions. First, the distribution with the next-smallest  $\chi^2$   
 290 was used, and a full reanalysis was made. Second, a  
 291  $Z = 1$  distribution with  $\chi^2/d.o.f. = \chi_{\text{min}}^2/d.o.f. + 1$   
 292 was selected, with a full reanalysis performed. A system-  
 293 atic difference of 3%–12% was found for the  $Z = 2$  frag-  
 294 ment yield in Au+Au collisions in the highest pseudorapidity  
 295 bins. In pseudorapidity and centrality bins where there  
 296 is a negligible higher- $Z$  yield, the MC class determined  
 297 from this analysis closely replicates the entire tail of the  
 298 singly-charged particles.

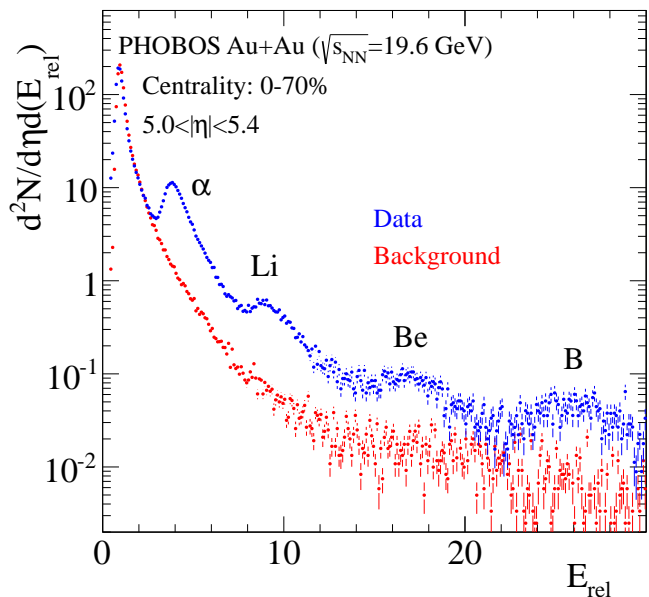


FIG. 3. (color online) The distribution of the relative energy loss in Au+Au collisions as  $\sqrt{s_{NN}} = 19.6$  GeV averaged over the centrality range 0%–70% and  $5.0 < |\eta| < 5.4$ . The blue distribution shows data, the error bars indicate statistical uncertainties only and the data are not corrected for acceptance. The red distribution shows the results from a MC simulation of singly-charged particles with spectator fragments explicitly excluded. See text for discussion.

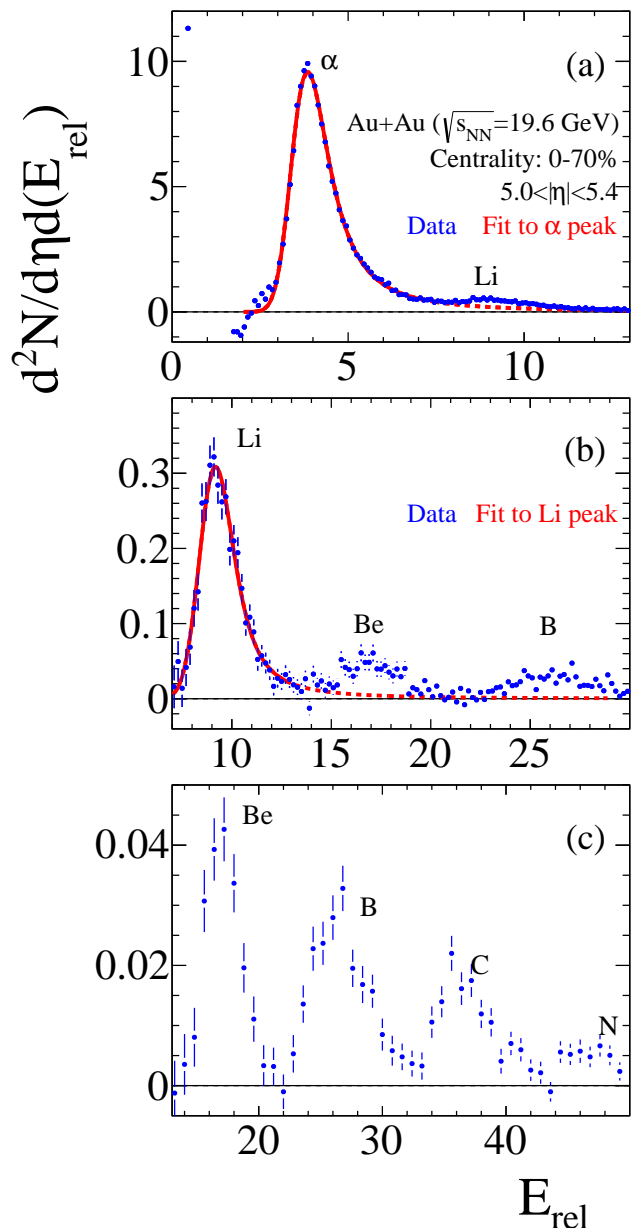


FIG. 4. (color online) Panel (a) shows the  $E_{\text{rel}}$  distribution after subtracting the  $Z=1$  component. The dominant peak at  $E_{\text{rel}} \sim 4$  corresponds to  $Z=2$  ( $\alpha$ ) fragments. The red line depicts the fit to determine fragment yields – the solid part shows the region over which the fit was made and the dashed is the extrapolation under the higher- $Z$  peaks. Panel (b) shows the same as (a) but with the contribution from the  $\alpha$  spectrum (red line in (a)) removed, highlighting the distribution from  $Z \geq 3$  fragments. The red line shows a fit to the Lithium peak, similar to that described in (a). Panel (c) shows the same as (b), but with the contribution from  $Z=3$  particles removed, and the  $x$ -axis is extended to show the presence of  $Z=6$  and  $Z=7$  fragments. The error bars are statistical only; data are not corrected for acceptance. See text for discussion.

## E. Extracting Fragment Yields

The measured  $E_{\text{rel}}$  distribution after subtraction of the fitted  $Z=1$  contribution is shown in Fig. 4a. The spectrum is dominated by the  $Z=2$  (referred to here as  $\alpha$ )<sup>1</sup> fragments. To determine the yield, the peak is fit with a convoluted Landau and Gaussian function (solid red line) in a region close to the  $\alpha$  peak, such that the fit range does not overlap the region where the Lithium peak is expected. The mean position in the fit is constrained to be the expected mean position for the  $\alpha$  fragments. The use of a Landau function is necessary to account for the high tail which partially resides underneath the higher mass peaks – in much the same way that the tail of the singly charged particles contributed to the  $\alpha$  peak, before subtraction. The total yield is calculated as the integral of this fit, extrapolated to encompass  $\alpha$  fragments appearing at high  $E_{\text{rel}}$ , for example under the Lithium peak (shown by the dashed red line). This extrapolation ultimately contributes less than 10% of the total yield, and the agreement between the raw data and the fit integrated over the same region ( $3 < E_{\text{rel}} < 6$ ) is better than 3%.

The full  $\alpha$  contribution to the energy loss spectrum is then subtracted (red line in Fig. 4a) to leave only  $Z \geq 3$  fragments (Fig. 4b). Next, with a similar procedure, the yield of Lithium fragments is determined using a Landau+Gaussian form (red solid and dashed lines), which is then subtracted from the relative energy loss spectrum. For the final distribution,  $Z \geq 4$  shown in Fig. 4c, the effect of the Landau tail is overpowered by the Gaussian width, and thus a two-Gaussian fit is used to extract the yields for Beryllium and Boron fragments. The mean positions used in this fit are constrained to be the expected position for each fragment. The number of these  $Z > 3$  fragments is only 1% of  $\alpha$  particles. As such, a small constant offset is allowed to account for possible uncertainties in subtracting  $\alpha$  and Lithium contributions to the spectrum, which could lead to over- or under-subtraction on the spectrum. For charges greater than five, the full centrality and  $\eta$  dependence is limited by the statistics collected in the single day of Au+Au running at the RHIC injection energy of  $\sqrt{s_{\text{NN}}} = 19.6$  GeV, and are therefore not included in this analysis. The same procedure is used to obtain  $Z=2$  and  $Z=3$  fragment yields in Cu+Cu collisions at  $\sqrt{s_{\text{NN}}} = 22.4$  GeV;  $Z > 3$  fragments are not observed, even given the larger statistics of the sample.

<sup>1</sup> Note:  $Z=2$  could imply either  ${}^3\text{He}$  or  ${}^4\text{He}$  ( $\alpha$ ). However, as the abundance of  ${}^4\text{He}$  is far greater, we refer to  $Z=2$  as  $\alpha$ .

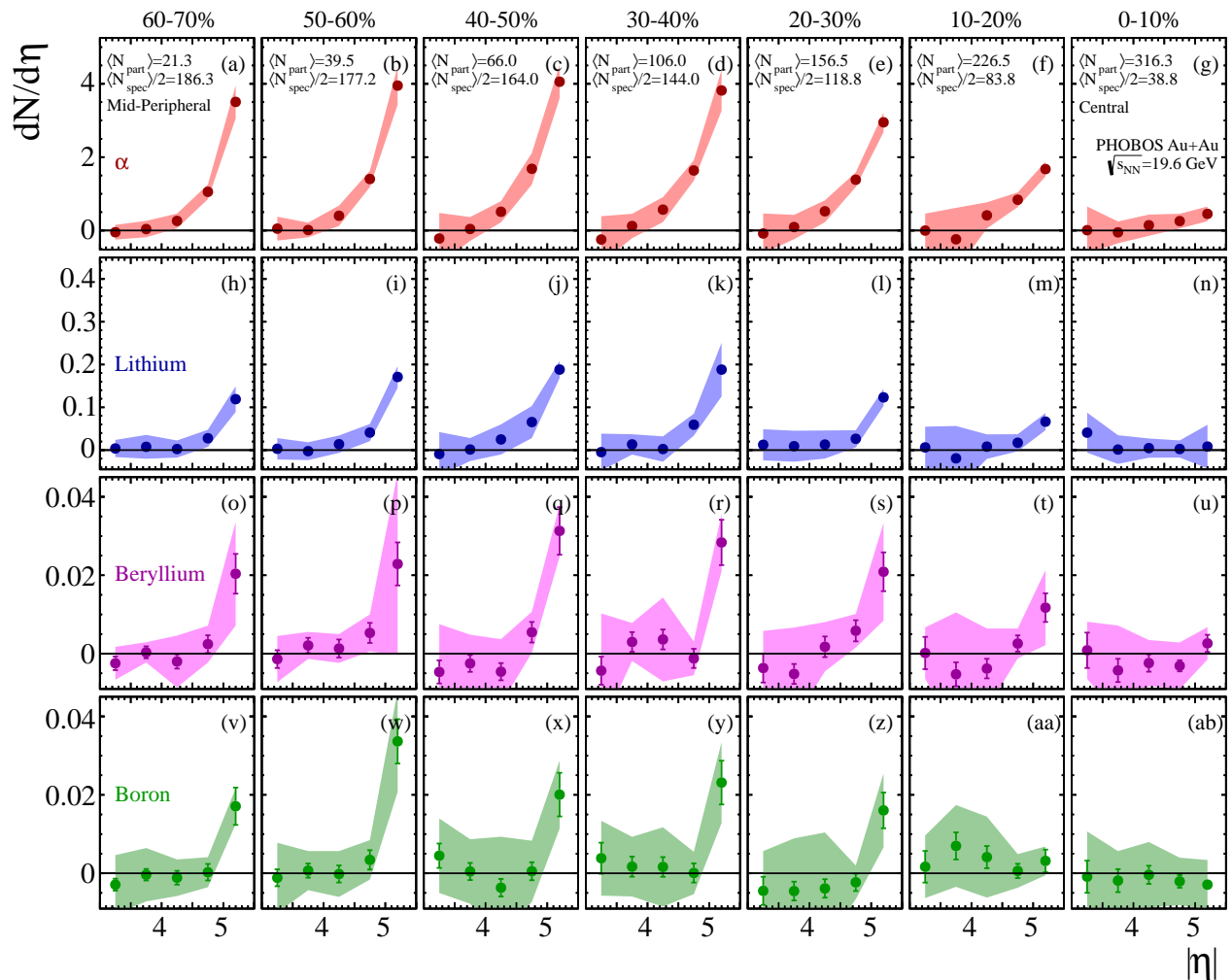


FIG. 5. (color online) Pseudorapidity dependence of  $\alpha$  (panels (a)-(g)), Lithium (h-n), Beryllium (o-u), and Boron (v-ab) fragments measured in Au+Au collisions at  $\sqrt{s_{NN}} = 19.6$  GeV. Data are presented in bins of centrality (more central in the rightmost panels) and are averaged over both hemispheres, i.e. the number of fragments per colliding nucleus. The error bars represent the statistical uncertainty, the error bands represent 90% C.L. systematic uncertainties in the yield.

### F. Corrections and Systematic Uncertainty

The data are corrected for acceptance via simulation which compares the number of tracks which impinge the detectors to all tracks in the full solid angle. As the  $Z=1$  “background” is explicitly subtracted, no further corrections are applied. The effect of absorption of the fragments in the 1 mm thick Beryllium beam pipe was evaluated via a GEANT simulation and was found to be negligible ( $<1\%$ ) as the fragments are high energy  $E_{\text{fragment}} \approx 9.8$  GeV (11.2 GeV) per nucleon for Au+Au (Cu+Cu) collisions.

Systematic uncertainties (90% C.L.) are evaluated by performing several checks, in addition to those due to the Landau  $Z=1$  background subtraction. The difference in the extracted yields measured independently in the positive and negative pseudorapidity regions of the PHO-

BOS detector is found to be 3%–11% for the  $\alpha$  yields in Au+Au collisions at the highest pseudorapidities, dependent on centrality. A shift of the measured energy scale in the  $E_{\text{rel}}$  calculation was applied ( $\pm 5\%$ ) which results in a 1%–8% uncertainty on the  $\alpha$  yield for the highest pseudorapidities. A total systematic uncertainty of 11% is assigned on the  $\alpha$  yield for the highest pseudorapidities in the 40%–50% centrality class. For larger fragments, an additional uncertainty due to the subtraction of the measured  $\alpha$  yield is estimated to be 1.5% for Lithium for the highest pseudorapidities in Au+Au collisions. The systematic uncertainties for 40%–50% Au+Au collisions at the highest pseudorapidities are 11%, 20%, and 45% for Lithium, Beryllium, and Boron, respectively.

It was also checked whether fragments could be due to interactions between collision products and the beam pipe, by measuring the number of  $Z=2$  fragments in

379  $\sqrt{s_{NN}} = 62.4$  GeV and 200 GeV data. Few were observed 431  
 380 in the former, while none were observed at the highest en-432  
 381 ergy. Should the high- $Z$  fragments have emanated from 433  
 382 dead and active detector material, notably the Beryllium 434  
 383 beam pipe, then the most central  $\sqrt{s_{NN}} = 200$  GeV data, 435  
 384 which has a larger multiplicity, would have included more 436  
 385 background than the lower energy data. Instead, we find 437  
 386 no evidence of  $Z = 2$  (or higher) fragments in the highest 438  
 387 energy data, indicating that such backgrounds from dead 439  
 388 material are negligible. 440

#### 389 IV. RESULTS I – PSEUDORAPIDITY 441 390 DEPENDENCE 442 443

391 Both the Au+Au and Cu+Cu data are divided into 444  
 392 five bins of pseudorapidity and seven and six bins of cen- 445  
 393 trality, respectively, corresponding to the top 70% (60%) 446  
 394 of nuclear inelastic cross-section. Figure 5 shows the 447  
 395 measured fragment multiplicity,  $dN/d\eta$ , as a function 448  
 396 of pseudorapidity (tabulated data are included in Ap- 449  
 397 pendix C), averaged over both hemispheres (i.e. the num- 450  
 398 ber of fragments per colliding nucleus) for Au+Au colli- 451  
 399 sions at  $\sqrt{s_{NN}} = 200$  GeV. The first row corresponds to  $\alpha$  452  
 400 fragments. Li, Be, and B fragments are shown in subse- 453  
 401 quent rows. The most central data (those with the least 454  
 402 number of spectators after the collision) are shown in the 455  
 403 rightmost column; the most peripheral are shown in the 456  
 404 leftmost column. As is apparent from this figure, there 457  
 405 are no  $Z > 1$  fragments for low pseudorapidities ( $|\eta| < 4.0$ ) 458  
 406 and only a small number of fragments are produced at 459  
 407 high centrality (0%–10% central). The lightest fragment 460  
 408 measured ( $\alpha$ ) is observed in each of the last three  $|\eta|$  bins, 461  
 409 Lithium fragments are observed in the highest two bins, 462  
 410 and Beryllium and Boron fragments are seen only in the 463  
 411 highest  $|\eta|$  bin. 464

412 Figure 6 shows the measured  $dN/d\eta$  for  $\alpha$  and Lithium 465  
 413 fragments in Cu+Cu collisions at  $\sqrt{s_{NN}} = 22.4$  GeV – 466  
 414 note that Lithium yields are scaled up by a factor of 10, 467  
 415 for clarity. Similarly to the Au+Au results, no spectator 468  
 416 fragments are observed in the low pseudorapidity region; 469  
 417 Lithium fragments are only observed in the highest pseu- 470  
 418 dorapidity bins. 471

#### 419 A. Comparison to Charged-particle pseudorapidity 472 420 density 473 474

421 PHOBOS has measured charged particle production in 475  
 422 the very forward region ( $|\eta| > \sim 3$ ) for Au+Au and Cu+Cu 476  
 423 collisions [16, 20, 21]. It was observed that the yield of 477  
 424 charged particles in this forward pseudorapidity region 478  
 425 is larger in the most peripheral collisions compared to 479  
 426 the central ones. In those analyses, no distinction was 480  
 427 made between singly- and multiply-charged particles, so 481  
 428 it was unclear how many of these particles were protons 482  
 429 (or deuterons or tritons) and how many were multiply- 483  
 430 charged fragments. Figure 7 (8) shows a comparison

between the pseudorapidity-averaged  $\alpha$  yield in Au+Au  
 (Cu+Cu) collisions measured in this analysis and the  
 charged-particle multiplicity ( $\eta > 3$ ) from the prior PHO-  
 BOS analyses [20]. For these centrality bins, the yield of  
 multiply-charged spectator fragments for both systems  
 is typically small ( $dN_\alpha/d\eta = 3.8 \pm 0.6$  in 30%–40% cen-  
 tral collisions at  $\sqrt{s_{NN}} = 19.6$  GeV) compared to the total  
 charged-particle multiplicity ( $18.5^{+9.2}_{-12.5}$ ). Therefore, the  
 majority of the particles in the forward region included in  
 the previously published analyses are singly-charged. Av-  
 eraged over centrality, the small abundance of multiply-  
 charged relative to singly-charged particles at the highest  
 pseudorapidity is also clearly seen in Fig. 3.

#### B. Comparison to Other Fragment Data

The number of  $\alpha$  particles measured by PHOBOS is  
 found to be similar to the yields measured in other ex-  
 periments. Figure 9 compares the measured  $dN_\alpha/d\eta$   
 from PHOBOS (filled circles with a band representing  
 the 90% C.L. systematic uncertainties in the yield) with  
 that from the KLMM [4] (Au projectile with beam energy  
 10.6 GeV per nucleon on a fixed emulsion (Em) target)  
 and KLM [7] (Pb projectile with beam energy 158 GeV  
 per nucleon on a fixed Pb target) collaborations<sup>2</sup>. Note  
 that the PHOBOS data are effectively a collision of a Au  
 projectile with  $E_{\text{beam}} = 9.8$  GeV per nucleon on a target  
 Au nucleus (albeit moving) where this energy is that of  
 a single beam in the collider, i.e.  $\sqrt{s_{NN}}/2$ . The data  
 are shifted along the  $x$ -axis in Fig. 9 by the correspond-  
 ing beam rapidity in each case. A detailed discussion  
 of the properties of this shifted variable ( $\eta' = \eta - y_{\text{beam}}$   
 or for symmetric collisions  $\eta' = |\eta| - y_{\text{beam}}$ ) is given in  
 Appendix A. Any impact of the difference of collision  
 energy should be fully compensated by this beam rapid-  
 ity shift, however as neither the collision systems nor the  
 event selection are identical some systematic differences  
 are expected. Small differences in yield between Au+Au  
 and Pb+Pb might arise from the fact that the Pb+Pb  
 collisions from the KLM analysis are on average more pe-  
 ripheral (covering 0%–100%) than the Au+Au collisions  
 (0%–70%) from this analysis. As such, any excess yield  
 in the PHOBOS measurements might be due to the miss-  
 ing 30% of the most peripheral events in this data set.  
 Moreover, we do not see any additional systematic effect  
 between our data and the KLMM data that collided Au  
 nuclei on Em (comprising much smaller nuclei: H, He, C,  
 Ag, and Br).

Although a large part of the  $\alpha$  yield is outside the ac-  
 ceptance of PHOBOS, the yield in the measured region  
 agrees reasonably well between experiments, and also il-  
 lustrates the relevance of limiting fragmentation for spec-

<sup>2</sup> The error bars shown for KLM and KLMM data in Fig. 9 are  
 based on the number of counts,  $N$ , in each  $\eta$  bin as  $\sqrt{N}$ .

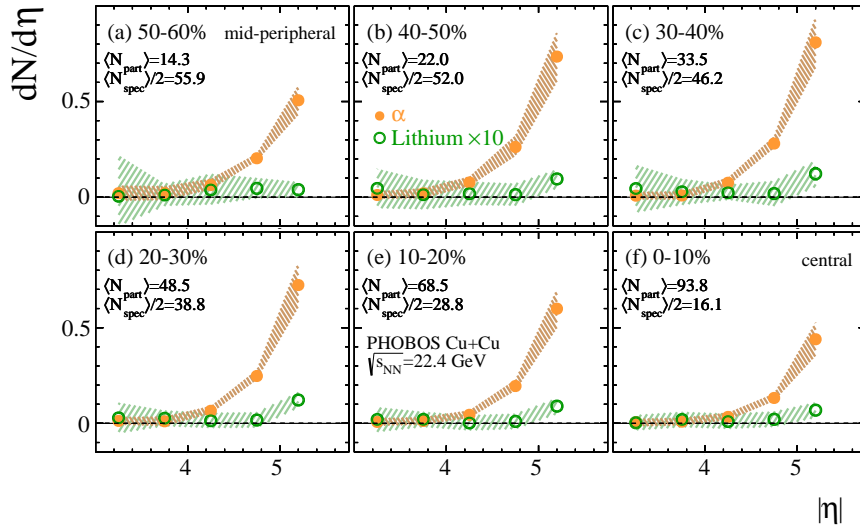


FIG. 6. (color online) Pseudorapidity dependence of  $\alpha$  (filled symbols) and Lithium fragments (open symbols) measured in Cu+Cu collisions at  $\sqrt{s_{NN}} = 22.4$  GeV. Lithium fragment yields are scaled up by a factor of 10 for clarity. Data are presented in bins of centrality and are averaged over both hemispheres, i.e. the number of fragments per colliding nucleus. The error bars represent the statistical uncertainty, the error bands represent 90% C.L. systematic uncertainties in the yield.

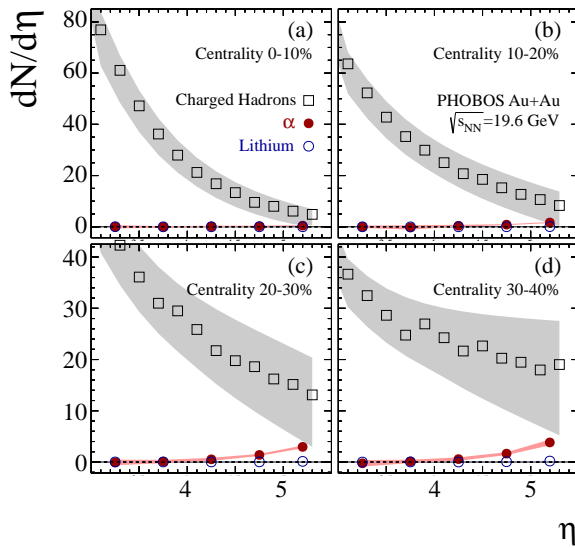


FIG. 7. (color online) Comparison between the PHOBOS charged particle multiplicity measured at positive  $\eta$  in Au+Au collisions at  $\sqrt{s_{NN}} = 19.6$  GeV and the yield of  $\alpha$  and Lithium fragments, averaged over positive and negative  $|\eta|$ . Panels (a), (b), (c), and (d) show the distributions in centrality bins 0%–10%, 10%–20%, 20%–30%, and 30%–40%, respectively. The open squares/light grey bands represents the PHOBOS multiplicity [20], filled (open) circles represent the measured  $\alpha$  (Li) yields.

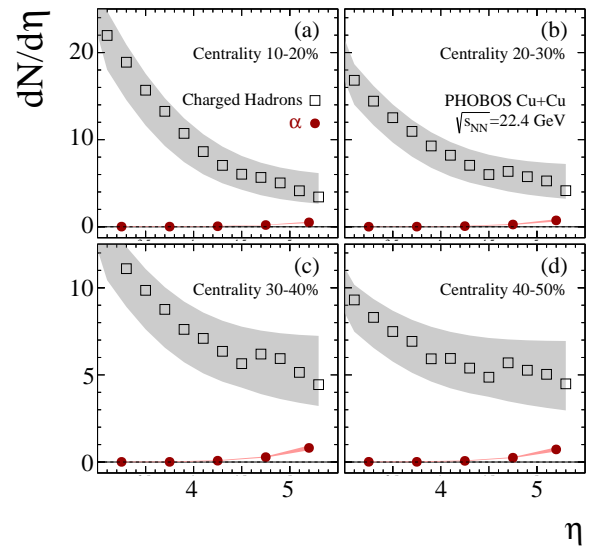


FIG. 8. (color online) Comparison between the measured PHOBOS charged particle multiplicity in Cu+Cu collisions at  $\sqrt{s_{NN}} = 22.4$  GeV and the yield of  $\alpha$  fragments. Panels (a), (b), (c), and (d) show the distributions in centrality bins 10%–20%, 20%–30%, 30%–40%, and 40%–50%, respectively. The open squares/light grey bands represents the PHOBOS multiplicity [20], filled circles represent the measured  $\alpha$  yields.

481 tators [16]. While Appendix A carefully describes why  
 482 beam rapidity is an appropriate scale to shift data at  
 483 different energies, it is more intuitive to compare boost-  
 484 invariant quantities such as  $dN/dp_T$ . Appendix B esti-  
 485 mates a conversion of the presented data into  $dN/dp_T$   
 486 as a function of  $p_T$ , and compares the resulting distribu-  
 487 tions with those estimated from lower energy collisions,  
 488 see Fig. 18. The Cu+Cu data are not shown as the ex-

489 pected difference in yield between Au (197) fragments  
 490 and Cu (63) fragments is large because of the difference  
 in mass – whereas the difference between Au (197) and  
 Pb (208) should be negligible.

## V. RESULTS II – CENTRALITY DEPENDENCE

Another way to look at this data is to examine the centrality dependence, shown in Fig. 10 for Au+Au col-

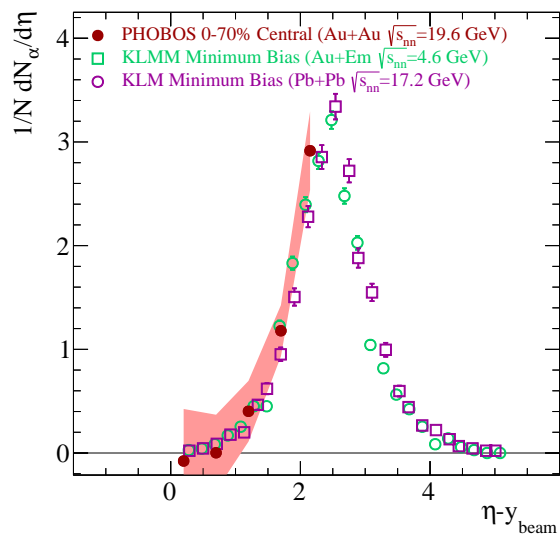


FIG. 9. (color online) Comparison of  $\alpha$  yields between PHOBOS data from Au+Au collisions ( $\sqrt{s_{NN}} = 19.6$  GeV) and Au+Em ( $\sqrt{s_{NN}} = 4.6$  GeV) [4] and Pb+Pb ( $\sqrt{s_{NN}} = 17.2$  GeV) [7] collisions. PHOBOS data are averaged over positive and negative  $\eta$  and over the most central 0%–70% cross-section (filled circles and shaded band which represent the 90% C.L. systematic uncertainties in the yield) for  $\alpha$  particles. The pseudorapidity ( $x$ -axis) is relative to the rest frame of the target nucleus for each energy, as discussed in Appendix A.

the associated data point systematic uncertainty. Figure 12 shows an example of a fit to peripheral (60%–70%) Au+Au ( $dN_\alpha/d\eta$ ) data to determine interpolated points at  $\eta' = 1.57$  and  $\eta' = 2.02$ . A similar fit is made to Cu+Cu data to determine an interpolated point at  $\eta' = 1.21$ .

A comparison of the centrality dependence of  $\alpha$  and Lithium yields for Au+Au and Cu+Cu is given in Fig. 13. The data are averaged over both hemispheres, representing the fragments from a single Gold (or Copper) nucleus. The yield of  $\alpha$  and Lithium fragments are shown versus  $N_{\text{spec}}/2$  from a single nucleus. Note that the  $x$ -axis is inverted such that central collisions are located rightmost on the figure. The magnitude of the yields of fragments is proportional to  $N_{\text{spec}}/2$  over a wide range of number of spectators. This behavior provides a simple explanation for the smaller number of fragments observed in peripheral Cu+Cu collisions compared to those from peripheral Au fragmentation. Modulo the drop-off for the most peripheral collisions, yields are approximately similar in the two systems for similar  $N_{\text{spec}}/2$ .

There is some evidence that, at the same  $N_{\text{spec}}/2$ , the yield of  $\alpha$  fragments is higher in Cu+Cu than in Au+Au, which is not apparent for Lithium. This is possibly due to a preference for emitting smaller fragments in the smaller Copper nucleus.

## B. Pseudorapidity and Centrality Dependence of Yields

The simultaneous pseudorapidity and centrality dependencies of the yields can be explored by use of ratios of data, to investigate whether the fragments appear at the same relative position for all centralities or not. Figure 14 shows the ratio of the yield of Li to He fragments evaluated at  $\eta' = 2.02$ . The three panels show the same data as a function of (a)  $N_{\text{spec}}/2$ , (b)  $N_{\text{part}}/2$ , and (c) the collision geometry ( $N_{\text{spec}}/2A$ ). Between Au+Au and Cu+Cu collisions, the Li/ $\alpha$  ratios clearly do not exhibit a scaling with either  $N_{\text{part}}/2$  (i.e. a similar Li/ $\alpha$  ratio at a similar  $N_{\text{part}}/2$ ) or with collision geometry. The collision geometry, defined as  $N_{\text{spec}}/2A$ , represents the fraction of total nuclear volume which interacts such that the overlap shape for each nucleus is roughly similar. A scaling with  $N_{\text{spec}}/2$  is suggested by the data – the decreased ratio would indicate that the emission of the lighter fragments is favored for fewer spectator nucleons from the collision system. However, the possibility that this ratio for each system is constant with centrality is not ruled out within the systematic uncertainty. For this scenario, the lower Cu+Cu ratio would indicate a more favorable emission of the lighter fragment in the Cu+Cu system than in Au+Au collisions.

From this data, one may attempt to draw a picture of the emission process for fragments. Unless the spectator nucleons acquire some  $p_T$  from intrinsic Fermi motion or the collision process itself, they would simply travel straight down the beam pipe until the magnetic field of

lisions at  $\sqrt{s_{NN}} = 19.6$  GeV. Here, the absence of fragments at low pseudorapidity is highlighted in the first two columns. Each  $|\eta|$  bin with a significant signal (panels c-e, i-j, o, t) shows a similar pattern: an increase of the yield for peripheral events, a turn-over for mid-central events, and finally an almost linear decrease with  $N_{\text{part}}/2$  toward the fully overlapping collisions. A similar dependence is also seen in the measured ZDC energy distribution versus centrality in the peripheral region at very high pseudorapidity, see for example Ref. [22].

In Cu+Cu collisions at  $\sqrt{s_{NN}} = 22.4$  GeV, a similar centrality dependence is observed for  $\alpha$  and Lithium fragments in Fig. 11.

## A. Comparison of Au+Au and Cu+Cu data

It should be noted that the relative coverage ( $\eta' \equiv |\eta| - y_{\text{beam}}$ ) of the detector is not quite the same for Au+Au and Cu+Cu collisions owing to the different beam rapidities:  $y_{\text{beam}} = 3.04$  (3.18) for Au+Au (Cu+Cu). Therefore, in comparing the two data sets, data points are evaluated at the same average  $\eta'$ , via an interpolation between measured points.

To evaluate the yield at each  $\eta'$ , a polynomial spline fit is made which smoothly connects the measured data points. The uncertainty in this method is evaluated with two different fits, which are found to be within 10% of

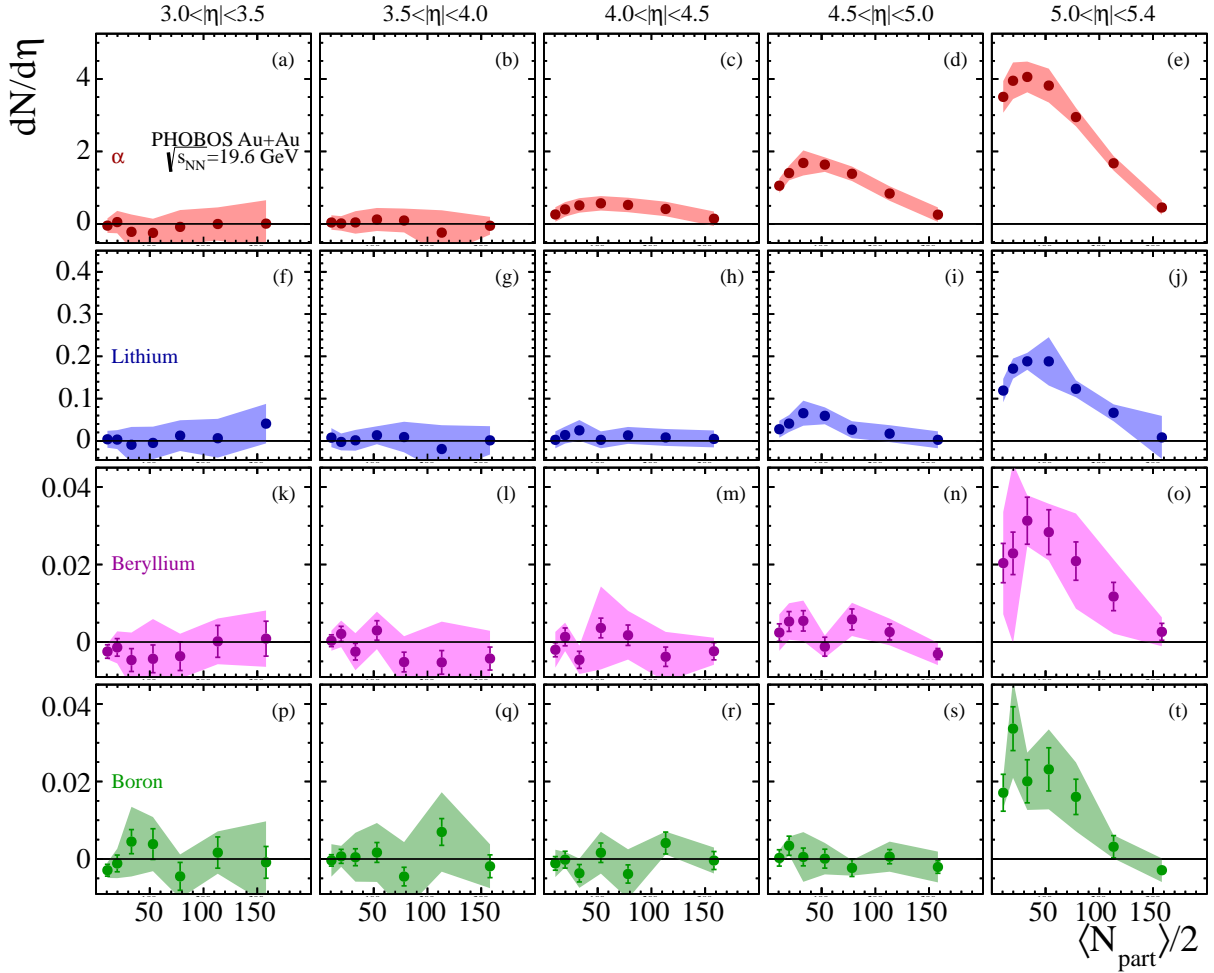


FIG. 10. (color online) Centrality dependence of  $\alpha$  (panels (a)-(e)), Lithium (f-j), Beryllium (k-o), and Boron (p-t) fragments measured in Au+Au collisions at  $\sqrt{s_{NN}} = 19.6$  GeV. Data are presented in bins of pseudorapidity,  $\eta$ , with the lowest  $\eta$  shown in the leftmost panels. The data are averaged over both hemispheres, i.e. the number of fragments per colliding nucleus. The error bars represent the statistical uncertainty, the error bands represent 90% C.L. systematic uncertainties in the yield. The errors associated with the centrality variables (here  $N_{\text{part}}/2$ ) are not shown on the figures, see Tables II–VII.

576 the RHIC steering magnets bent them away. In such a case, they would not be visible in the detector as these magnets are located too far from the apparatus to have had any influence on the fragments. The movement of the fragments must be connected to the nucleus and/or be the result of the collision.

582 In the simplest scenario, the fragments would move outward due to their intrinsic (precollision) motion, without further interaction. This, however, would result in the centrality and pseudorapidity dependencies being coupled from each other. Specifically, the data in every pseudorapidity interval should have the same centrality dependence (although with different yields); this is not seen in the data. Figures 15 and 16 show the ratio of yields evaluated at  $\eta' = 1.57$  and  $\eta' = 1.21$ , respectively, divided by the yield at  $\eta' = 2.02$ , for both Au+Au and Cu+Cu collision systems. The three panels show the same data as a function of (a)  $N_{\text{spec}}/2$ , (b)  $N_{\text{part}}/2$ , and

(c) the collision geometry.

The ratios in Figs. 15 and 16 are not constant as the number of  $\alpha$  particles in each  $\eta'$  range ( $\eta' = 1.57$  and  $1.21$ , respectively) diminishes (compared to the reference at  $\eta' = 2.02$ ) with decreasing centrality. Effectively, the  $\alpha$  particles are moving out of the acceptance of the detector for more peripheral collisions and the average deflection away from the beam direction increases for more central collisions. Such a deflection is suggestive of a specific dependence of transverse momentum acquired by the fragments. The same effect is also observed in Cu+Cu collisions. For fragments moved into the acceptance of PHOBOS due to intrinsic (precollision) motion, one would expect no centrality dependence of these ratios, i.e. all flat. Comparing the Cu+Cu and Au+Au data in the three scaling scenarios, it is apparent that these ratios favor a scaling with  $N_{\text{part}}/2$ , which is perhaps counter-intuitive as these spectators are often considered to be

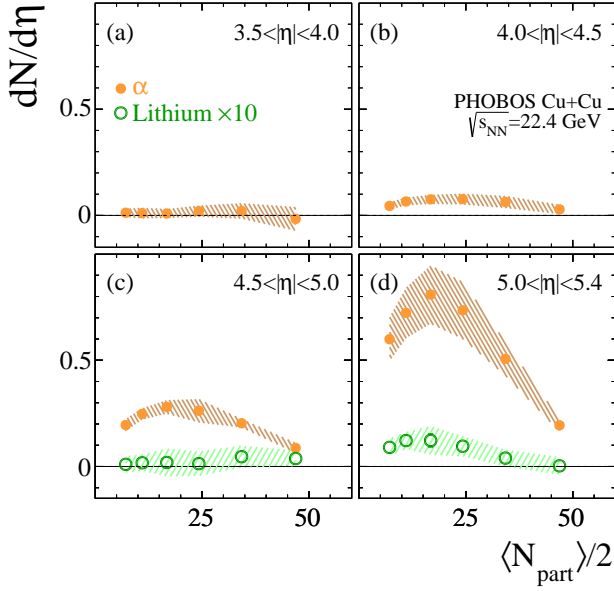


FIG. 11. (color online) Centrality dependence of  $\alpha$ -fragments (filled symbols) for  $\sqrt{s_{NN}} = 22.4$  GeV Cu+Cu collisions for four  $|\eta|$  bins (a-d). For clarity, Lithium (open symbols) are scaled up by a factor of 10 and are only shown for the highest two pseudorapidity bins (panels (c) and (d)). The data are averaged over both hemispheres, i.e. the number of fragments per colliding nucleus. The error bars (typically smaller than the symbol height) represent the statistical uncertainty, the error bands represent 90% C.L. systematic uncertainties in the yield.

612 independent of interactions in the hot participant zone.

## 613 VI. CONCLUSION

614 In conclusion, nuclear fragments ( $Z > 1$ ) have been ob-  
 615 served up to  $Z = 7$  using the extensive reach in pseudo-  
 616 rapidity of the PHOBOS detector. The pseudorapid-  
 617 ity and centrality dependence is shown for fragments  
 618 up to  $Z = 5$  only for Au+Au; for Cu+Cu this study  
 619 is restricted to  $Z = 2$  and 3. Fragments from Au+Au  
 620 ( $\sqrt{s_{NN}} = 19.6$  GeV) and Cu+Cu ( $\sqrt{s_{NN}} = 22.4$  GeV)  
 621 collisions have sufficiently low longitudinal momentum that  
 622 even fragments which have a modest  $p_T$  are deflected  
 623 into the PHOBOS apparatus. The yield of  $\alpha$  fragments  
 624 is observed to be similar to that measured in other exper-  
 625 iments over a range of energies if evaluated at the same  
 626 value of  $\eta - y_{beam}$ . As a function of centrality, the yield  
 627 of  $\alpha$  and Lithium fragments is found to approximately  
 628 scale with the number of spectators in the collision. The  
 629 centrality dependence of ratios of  $\alpha$  fragment yields at  
 630 different pseudorapidities illustrates that these fragments  
 631 move out of the acceptance of the detector for more pe-  
 632 ripheral collisions. In comparing Cu+Cu and Au+Au ra-  
 633 tios, a scaling with the number of participants is favored,  
 634 suggesting an influence of the hot participant zone with

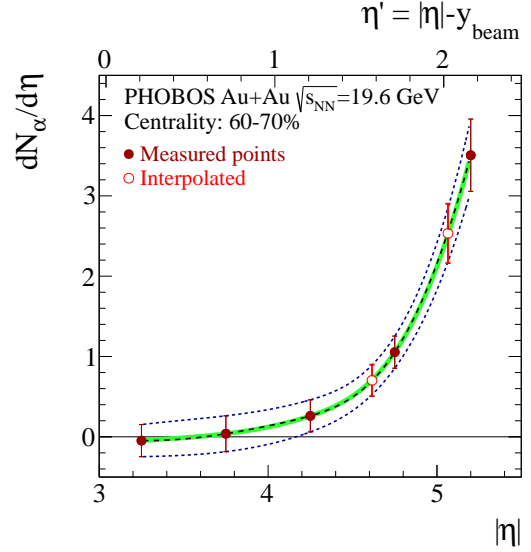


FIG. 12. (color online) Spline polynomial fits (lines) to  $\alpha$  yields from Au+Au peripheral (60%–70%) data (filled circles). Interpolated points at  $\eta' = 1.57$  and  $\eta' = 2.02$  are shown as open circles. The scale on the upper  $x$ -axis shows  $\eta' \equiv |\eta| - y_{beam}$ . The dashed and green lines show fits using polynomials of different order. The outer dotted lines represent a fit to points at the extreme of the systematic uncertainty bands.

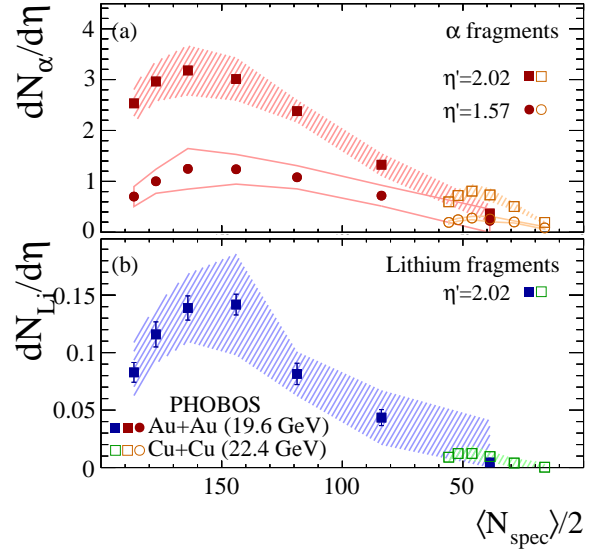


FIG. 13. (color online) Centrality dependence of  $\alpha$  (panel (a)) and Lithium yields (b) in  $\sqrt{s_{NN}} = 19.6$  GeV Au+Au (filled symbols) and 22.4 GeV Cu+Cu (open symbols) collisions. Note that the centrality variable is not  $N_{part}/2$  but  $N_{spec}$  from a single nucleus – see text for details – and the  $x$ -axis runs backwards, central collisions are the rightmost data points. The  $\alpha$  data are evaluated at  $\eta' = 1.57$  (circles/unfilled systematic bands) and  $\eta' = 2.02$  (squares/filled systematic bands). Lithium yields are only shown for  $\eta' = 2.02$ . The bands represent 90% C.L. systematic uncertainties in the yield.

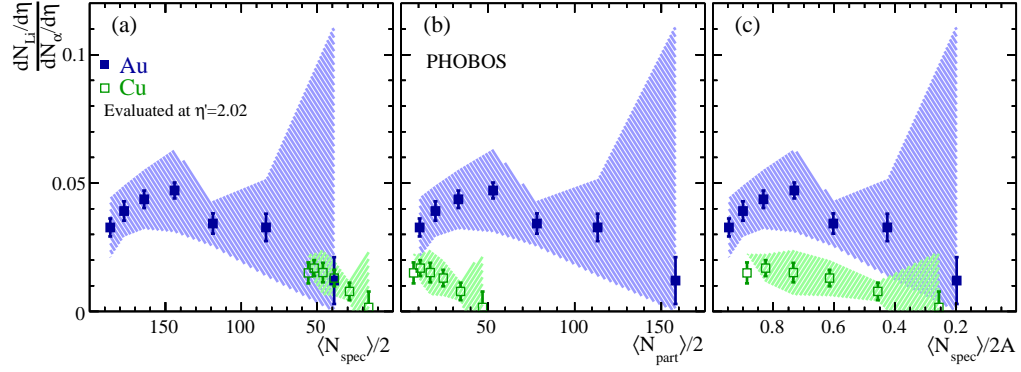


FIG. 14. (color online) Centrality dependence of the yield of Lithium nuclei divided by that of  $\alpha$  particles evaluated at  $\eta' = 2.02$ . Au+Au (filled symbols) and Cu+Cu (open symbols) collision data are shown as a function of (a)  $N_{\text{spec}}/2$ , (b)  $N_{\text{part}}/2$ , and (c) the collision geometry ( $N_{\text{spec}}/2A$ ). The bands represent 90% C.L. systematic uncertainties in the ratio.

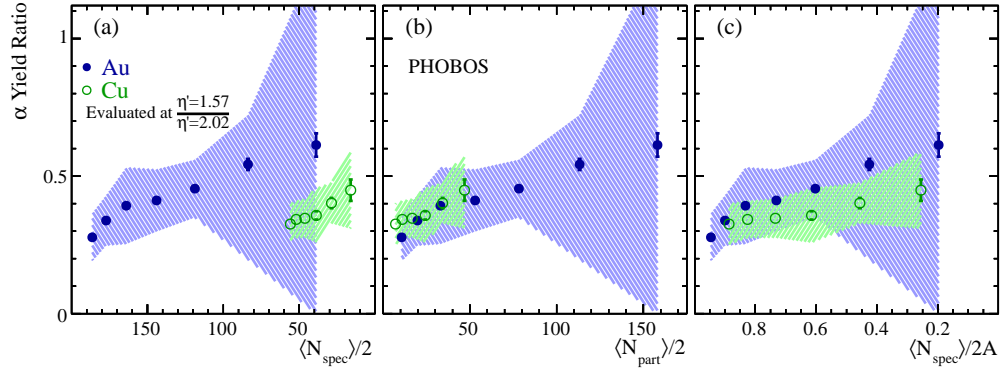


FIG. 15. Centrality dependence of the yield of  $\alpha$ -particles evaluated at  $\eta' = 1.57$  divided by the yield measured at  $\eta' = 2.02$ . Au+Au (filled symbols) and Cu+Cu (open symbols) collision data are shown as a function of (a)  $N_{\text{spec}}/2$ , (b)  $N_{\text{part}}/2$ , and (c) the collision geometry ( $N_{\text{spec}}/2A$ ). The bands represent 90% C.L. systematic uncertainties in the ratio.

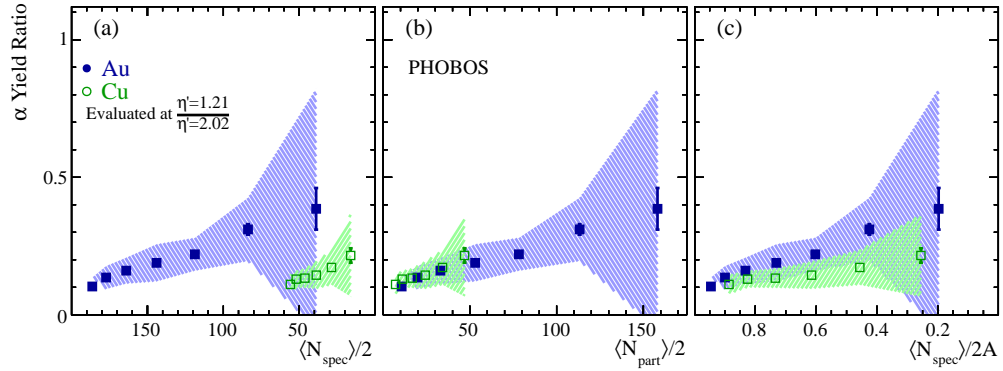


FIG. 16. Centrality dependence of the yield of  $\alpha$ -particles evaluated at  $\eta' = 1.21$  divided by the yield measured at  $\eta' = 2.02$ . Au+Au (filled symbols) and Cu+Cu (open symbols) collision data are shown as a function of (a)  $N_{\text{spec}}/2$ , (b)  $N_{\text{part}}/2$ , and (c) the collision geometry ( $N_{\text{spec}}/2A$ ). The bands represent 90% C.L. systematic uncertainties in the ratio.

635 the nonparticipating spectators.

velocity,  $\beta_z$ :

$$y \equiv \frac{1}{2} \ln \left( \frac{E + p_z}{E - p_z} \right) = \tanh^{-1} \left( \frac{p_z}{E} \right) = \tanh^{-1} \beta_z, \quad (\text{A1})$$

## 636 Appendix A: Relating $y$ and $\eta$

Rapidity,  $y$ , is defined in Eq. A1 from Ref. [23] and has a simple one-to-one relationship with the longitudinal

637 where  $E$  is the total energy of the particle and  $p_z$  is the longitudinal momentum, i.e. the component along the beam direction. In addition, rapidity has the well-known 639

property that longitudinal boosts are simply additive, where rapidity differences,  $y_1 - y_2$ , are invariant under longitudinal boosts.

In some cases, such as in the PHOBOS multiplicity detector, only a particle's direction ( $\theta$  – polar angle and  $\phi$  – azimuthal angle) is accessible, and not the actual momentum. In such cases we use the pseudorapidity variable,  $\eta$  – Eq. A2, from Ref. [23]:

$$\eta \equiv -\ln(\tan(\theta/2)), \quad (\text{A2})$$

where  $\theta$  is the polar angle with respect to the beam direction. In order to relate these two quantities, one can use two identities from Ref. [23]:

$$p_z = m_T \sinh y, \quad (\text{A3})$$

where  $m_T$  is the transverse mass, defined as  $m_T^2 = m^2 + p_T^2$ , and

$$p_z = p_T \sinh \eta, \quad (\text{A4})$$

which can be derived from

$$\sinh \eta = \cot \theta. \quad (\text{A5})$$

These identities result in the relation:

$$\sinh \eta = (\sinh y) \sqrt{1 + \frac{m^2}{p_T^2}}. \quad (\text{A6})$$

### Mapping $\eta'$ to $y'$ versus $p_T/m$ .

The resulting relation between  $y$  and  $\eta$  (Eq. A6) has many implications:

1.  $\eta/y \geq 1$ , which leads directly to
2.  $y$  and  $\eta$  have the same sign, and
3.  $|\eta| > |y|$ .

One can examine two limits of this relation. First, in the limit of small  $\eta$  (and therefore also small  $y$ ),  $\sinh \eta \rightarrow \eta$  and therefore:

$$\eta \approx y \sqrt{1 + \frac{m^2}{p_T^2}}. \quad (\text{A7})$$

Second, and more importantly for this work, at large  $y$  (and therefore also large  $\eta$ ) one can write:

$$\sinh y = e^y(1 - e^{-2y})/2 \rightarrow e^y/2. \quad (\text{A8})$$

Using Eq. A6 this leads to:

$$\eta \approx y + \frac{1}{2} \ln \left( 1 + \frac{m^2}{p_T^2} \right). \quad (\text{A9})$$

Finally, using the definitions:  $\eta' \equiv \eta - y_{\text{beam}}$  and  $y' \equiv y - y_{\text{beam}}$ :

$$\eta' \approx y' + \frac{1}{2} \ln \left( 1 + \frac{m^2}{p_T^2} \right). \quad (\text{A10})$$

Equation A10 holds the key information in the relations between  $y'$  and  $\eta'$ : at large  $y$ , an  $\eta'$  bin corresponds to a fixed region in  $(y', p_T/m)$  space, independent of  $y_{\text{beam}}$ . Therefore, this formulation represents the best way to compare  $dN/d\eta$  distributions measured at various beam energies.

One can estimate the validity of this approximation by calculating the absolute error at each rapidity. An upper bound on the absolute error from Eq. A10 is given by  $|\ln(1 - e^{-2y})| \approx e^{-2y}$ . For  $y > 2$  ( $> 3$ ,  $> 5$ ), the error is estimated to be less than 0.02 ( $< 2.5 \times 10^{-3}$ ,  $< 5.0 \times 10^{-5}$ ) units. Even for  $y = 1$ , the error in the “large- $y$ ” approximation is less than 0.145.

To further illustrate this approximation, for a fixed window in  $\eta'$  ( $1.8 < \eta' < 2.0$ ), Fig. 17 shows the  $y'$ - $p_T/m$  acceptance. Panels (a-c) show bands representing the different beam energies used in this paper: (a)  $\sqrt{s_{NN}} = 19.6$  GeV, and 22.4 GeV representing Au+Au and Cu+Cu collision data, respectively, measured by PHOBOS, (b)  $E_{\text{beam}} = 10.6$  GeV collisions of Au nuclei on an emulsion target (Em) measured by KLMM, and (c)  $E_{\text{beam}} = 158$  GeV collisions of Pb nuclei on a stationary Pb target as measured by KLM. Panel (d) shows an overlay of all distributions. The arrows represent midrapidity (i.e.  $y=0$  and  $\eta=0$ ). The three lowest energy bands (PHOBOS and KLMM) almost entirely overlap owing to their very similar beam energies (or equivalently  $y_{\text{beam}}$ ).

In general, to compare results in the rest frame of the beam particle, PHOBOS has used  $\eta'$  to compare pseudorapidity distributions in the “fragmentation” or “extended longitudinal scaling” region among data at different energies ( $dN_{ch}/d\eta$  [16, 20, 24–26], and also for the first and second harmonic of the Fourier decomposition of the azimuthal angle distribution – known as  $v_1$  [1] and  $v_2$  [27], respectively). This is roughly confined to the  $|\eta| > 2$  region, so, as shown,  $\eta'$  is ideally suited for this, second only to  $y'$  itself.

### Limitations

As Fig. 17 suggests, there are limitations in this simplification. There are two important considerations in using  $\eta'$  rather than  $y'$ . The first is that the shape in  $(y', p_T/m)$  space is non-intuitive and does *not* generally correspond to  $\eta' = y'$  except when  $p_T \gg m$ . Therefore, generally interpreting an  $\eta'$  distribution as equivalent to  $y'$  can be seriously incorrect in certain cases. The second issue is that there can, in principle, be some contamination to high- $\eta$  from particles with very low  $p_T$  and  $y$  that is not quite beam-energy-independent. Usually the fact that these particles would have to come from very low

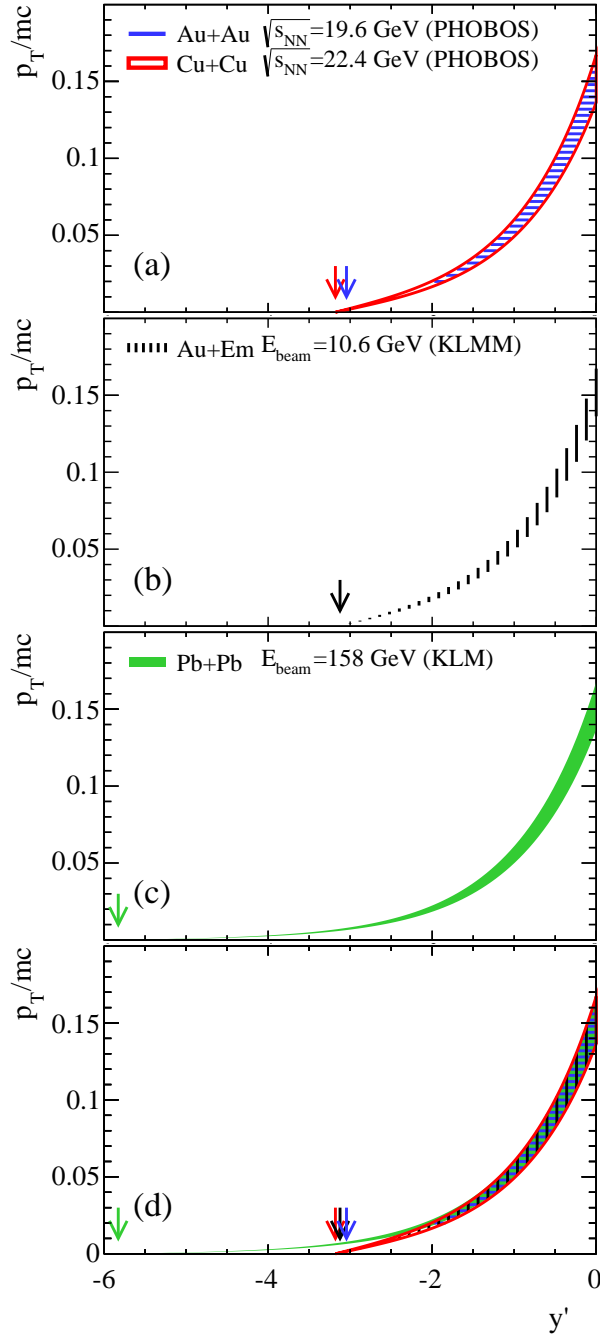


FIG. 17. (color online)  $p_T/m$ - $y'$  acceptance for a fixed  $1.8 < \eta' < 2.0$  window. The upper (lower) bound on each band corresponds to  $\eta' = 1.8$  ( $2.0$ ). The top three panels (a-c) show the acceptance for PHOBOS ( $\sqrt{s_{NN}} = 19.6$  GeV, and  $22.4$  GeV), KLMM ( $E_{\text{beam}} = 10.6$  GeV), and KLM ( $E_{\text{beam}} = 158$  GeV) respectively. The lower panel (d) shows an overlay of all distributions. The arrows represent midrapidity ( $y=0$  and  $\eta=0$ ) at each energy. See text for discussion.

all go to 0 at  $p_T=0$ . In particular, for the region of  $\eta' > 0$ , the mid-rapidity contribution is at *particularly* low  $p_T$ . For  $\alpha$  particles in this work, the contamination from mid-rapidity can be expected to be negligible.

When comparing collider data to fixed target data, there is an extra consideration. For the positive side  $\eta' = \eta - y_{\text{beam}}$ , each  $\eta'$  bin contains contributions from all positive values of  $y$ . In the case of the collider kinematics this stops at mid-rapidity. In the case of fixed target kinematics this could, in principle, include contributions from particles near the target rapidity (which is 0). Therefore, some small contamination of  $\alpha$  particles emitted at very low  $p_T$  from the target rather than from the  $Au$  beam could occur. Again, this is expected to be negligible, despite the extent in  $\eta$ , since it is at very low  $p_T$  and a very narrow window in  $p_T$ .

### Appendix B: Estimation of $dN/dp_T$

The quantity  $dN/dp_T$  is known to be invariant under longitudinal boosts and may provide an additional check on scaling between data samples at different energies. The measurement of  $p_T$  is not possible at forward pseudorapidity in PHOBOS, so an estimate is needed. It is assumed that the longitudinal momentum of the spectator nucleons does not change during the collision. Given this assumption, one can calculate the transverse momentum as:

$$p_T = \frac{m \sinh(y_{\text{beam}})}{\sinh(\eta)} \quad (\text{B1})$$

where  $m$  is the mass of the particle of interest ( $\alpha$ ). Differentiating Eq. B1 yields the Jacobian needed to transform  $dN/d\eta \rightarrow dN/dp_T$ :

$$\frac{d\eta}{dp_T} = \frac{d\eta'}{dp_T} = -\frac{\tanh(\eta)}{p_T} \quad (\text{B2})$$

Using these relations (Eq. B1 and B2), one can transform  $dN/d\eta$  as a function of  $\eta$  into  $dN/dp_T$  as a function of  $p_T$ . As a reminder, this is an estimate of both quantities and is not a precise measurement. Figure 18 shows a comparison of the estimated  $dN/dp_T$  versus  $p_T$  for 0%-70% central Au+Au collisions at  $\sqrt{s_{NN}} = 19.6$  GeV. For comparison, the same technique is used to transform the data from Au+Em ( $\sqrt{s_{NN}} = 4.6$  GeV) [4] and Pb+Pb ( $\sqrt{s_{NN}} = 17.2$  GeV) [7] collisions (i.e. from the data shown in Fig. 9). The data agree well within the uncertainties described above. Figure 19 shows a comparison between central (closed symbols) and mid-peripheral (open) Au+Au collisions. The Cu+Cu data are not shown as the expected difference in yield between Au (197) fragments and Cu (63) fragments is large because of the difference in mass – whereas the difference between Au (197) and Pb (208) should be negligible.

<sup>699</sup>  $p_T$  helps to suppress them since the  $d^2N/dydp_T$  yields

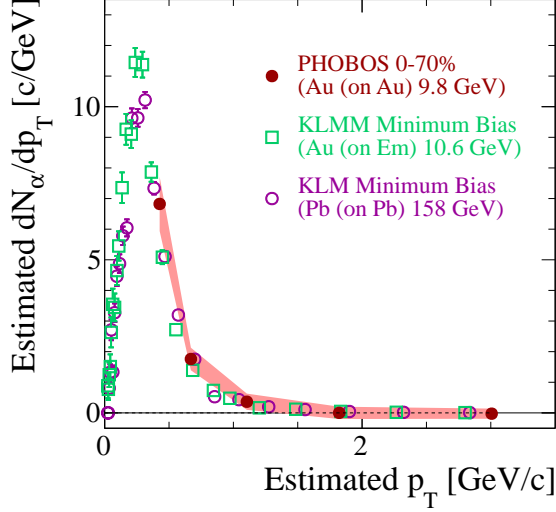


FIG. 18. (color online) Estimated  $dN/dp_T$  distribution for  $\alpha$  fragments near beam rapidity for 0%–70% central Au+Au collisions at  $\sqrt{s_{NN}} = 19.6$  GeV. Estimation procedure is described in the text. For comparison, Au+Em ( $\sqrt{s_{NN}} = 4.6$  GeV) [4] and Pb+Pb ( $\sqrt{s_{NN}} = 17.2$  GeV) [7] collisions are shown, using the same estimation method.

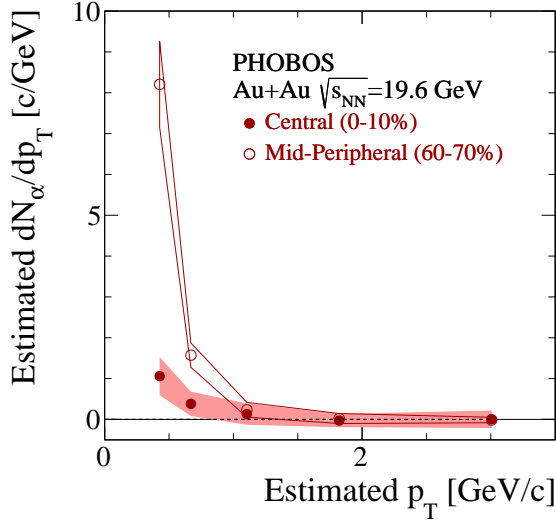


FIG. 19. (color online) Estimated  $dN/dp_T$  distribution for  $\alpha$  fragments near beam rapidity for Au+Au collisions at  $\sqrt{s_{NN}} = 19.6$  GeV. Estimation procedure is described in the text. The open and closed symbols represent central (0%–10%) and mid-peripheral (60%–70%) collisions, respectively.

TABLE I.  $N_{\text{part}}$  values determined from a Glauber model calculation for Au+Au ( $\sqrt{s_{NN}} = 19.6$  GeV) and Cu+Cu ( $\sqrt{s_{NN}} = 22.4$  GeV) collisions. Uncertainties are 90% C.L. systematic.

Centrality Bin (%)	Number of Participants	
	Au+Au	Cu+Cu
0-10	$316.3 \pm 9.9$	$93.8 \pm 3.0$
10-20	$226.5 \pm 8.0$	$68.5 \pm 3.0$
20-30	$156.5 \pm 7.0$	$48.5 \pm 3.0$
30-40	$106.0 \pm 7.0$	$33.5 \pm 3.0$
40-50	$66.0 \pm 4.7$	$22.0 \pm 3.0$
50-60	$39.5 \pm 3.0$	$14.3 \pm 3.0$
60-70	$21.3 \pm 3.0$	–

### Appendix C: Tables of data

Table I shows the  $N_{\text{part}}$  values determined from a Glauber model calculation for Au+Au ( $\sqrt{s_{NN}} = 19.6$  GeV) and Cu+Cu ( $\sqrt{s_{NN}} = 22.4$  GeV) collisions.

Tables II–V and VI–VII contain the corrected  $dN_{\text{particle}}/d\eta$  yields as function of collision centrality for Au+Au ( $\sqrt{s_{NN}} = 19.6$  GeV) and Cu+Cu ( $\sqrt{s_{NN}} = 22.4$  GeV) collisions, respectively. Note that for clarity some values are scaled up by powers of 10.

### ACKNOWLEDGMENTS

This work was partially supported by U.S. DOE grants DE-AC02-98CH10886, DE-FG02-93ER40802, DE-FG02-94ER40818, DE-FG02-94ER40865, DE-FG02-99ER41099, and DE-AC02-06CH11357, by U.S. NSF grants 9603486, 0072204, and 0245011, by Polish National Science Center grant DEC-2013/08/M/ST2/00320, by NSC of Taiwan Contract NSC 89-2112-M-008-024, and by Hungarian OTKA grant (F 049823).

[1] B. B. Back *et al.*, (PHOBOS Collaboration), Phys. Rev. Lett. **97**, 012301 (2006).

[2] M. I. Adamovich *et al.* (EMU-01 Collaboration), Phys.

TABLE II.  $dN_\alpha/d\eta$  measured in Au+Au collisions at  $\sqrt{s_{NN}} = 19.6$  GeV. Uncertainties are  $1-\sigma$  statistical and 90% C.L. systematic.

Centrality Bin (%)	Yield				
	$3.0 <  \eta  < 3.5$	$3.5 <  \eta  < 4.0$	$4.0 <  \eta  < 4.5$	$4.5 <  \eta  < 5.0$	$5.0 <  \eta  < 5.4$
0-10	$0.01 \pm 0.03 \pm 0.65$	$-0.05 \pm 0.02 \pm 0.30$	$0.14 \pm 0.01 \pm 0.29$	$0.26 \pm 0.01 \pm 0.20$	$0.45 \pm 0.02 \pm 0.20$
10-20	$-0.00 \pm 0.02 \pm 0.46$	$-0.24 \pm 0.02 \pm 0.86$	$0.41 \pm 0.02 \pm 0.36$	$0.84 \pm 0.02 \pm 0.20$	$1.67 \pm 0.03 \pm 0.20$
20-30	$-0.08 \pm 0.02 \pm 0.55$	$0.09 \pm 0.01 \pm 0.33$	$0.52 \pm 0.02 \pm 0.30$	$1.38 \pm 0.02 \pm 0.20$	$2.95 \pm 0.04 \pm 0.27$
30-40	$-0.25 \pm 0.02 \pm 0.64$	$0.12 \pm 0.01 \pm 0.33$	$0.57 \pm 0.02 \pm 0.34$	$1.64 \pm 0.02 \pm 0.28$	$3.82 \pm 0.04 \pm 0.56$
40-50	$-0.22 \pm 0.02 \pm 0.70$	$0.04 \pm 0.01 \pm 0.33$	$0.51 \pm 0.02 \pm 0.29$	$1.68 \pm 0.02 \pm 0.43$	$4.06 \pm 0.04 \pm 0.45$
50-60	$0.05 \pm 0.01 \pm 0.33$	$0.01 \pm 0.01 \pm 0.20$	$0.40 \pm 0.01 \pm 0.28$	$1.40 \pm 0.02 \pm 0.22$	$3.95 \pm 0.04 \pm 0.52$
60-70	$-0.05 \pm 0.01 \pm 0.20$	$0.04 \pm 0.01 \pm 0.22$	$0.26 \pm 0.01 \pm 0.20$	$1.05 \pm 0.02 \pm 0.20$	$3.51 \pm 0.04 \pm 0.45$

TABLE III.  $dN_{Li}/d\eta$  measured in Au+Au collisions at  $\sqrt{s_{NN}} = 19.6$  GeV. Uncertainties are  $1-\sigma$  statistical and 90% C.L. systematic. Yields are scaled up by a factor of 10 for clarity.

Centrality Bin (%)	Yield $\times 10$				
	$3.0 <  \eta  < 3.5$	$3.5 <  \eta  < 4.0$	$4.0 <  \eta  < 4.5$	$4.5 <  \eta  < 5.0$	$5.0 <  \eta  < 5.4$
0-10	$0.41 \pm 0.07 \pm 0.47$	$0.01 \pm 0.05 \pm 0.34$	$0.05 \pm 0.03 \pm 0.22$	$0.03 \pm 0.03 \pm 0.20$	$0.08 \pm 0.04 \pm 0.51$
10-20	$0.06 \pm 0.07 \pm 0.48$	$-0.19 \pm 0.05 \pm 0.76$	$0.08 \pm 0.04 \pm 0.29$	$0.17 \pm 0.04 \pm 0.20$	$0.66 \pm 0.07 \pm 0.20$
20-30	$0.12 \pm 0.06 \pm 0.36$	$0.09 \pm 0.04 \pm 0.36$	$0.13 \pm 0.04 \pm 0.33$	$0.26 \pm 0.04 \pm 0.20$	$1.23 \pm 0.09 \pm 0.20$
30-40	$-0.05 \pm 0.06 \pm 0.43$	$0.13 \pm 0.04 \pm 0.24$	$0.02 \pm 0.04 \pm 0.30$	$0.59 \pm 0.05 \pm 0.26$	$1.88 \pm 0.11 \pm 0.63$
40-50	$-0.09 \pm 0.05 \pm 0.51$	$0.01 \pm 0.03 \pm 0.27$	$0.25 \pm 0.04 \pm 0.35$	$0.66 \pm 0.05 \pm 0.37$	$1.88 \pm 0.11 \pm 0.20$
50-60	$0.03 \pm 0.04 \pm 0.25$	$-0.02 \pm 0.03 \pm 0.21$	$0.14 \pm 0.03 \pm 0.20$	$0.41 \pm 0.05 \pm 0.20$	$1.71 \pm 0.11 \pm 0.25$
60-70	$0.04 \pm 0.03 \pm 0.20$	$0.08 \pm 0.02 \pm 0.28$	$0.02 \pm 0.03 \pm 0.20$	$0.28 \pm 0.04 \pm 0.20$	$1.19 \pm 0.10 \pm 0.30$

TABLE IV.  $dN_{Be}/d\eta$  measured in Au+Au collisions at  $\sqrt{s_{NN}} = 19.6$  GeV. Uncertainties are  $1-\sigma$  statistical and 90% C.L. systematic. Yields are scaled up by a factor of 100 for clarity.

Centrality Bin (%)	Yield $\times 100$				
	$3.0 <  \eta  < 3.5$	$3.5 <  \eta  < 4.0$	$4.0 <  \eta  < 4.5$	$4.5 <  \eta  < 5.0$	$5.0 <  \eta  < 5.4$
0-10	$0.09 \pm 0.45 \pm 0.73$	$-0.43 \pm 0.30 \pm 1.14$	$-0.24 \pm 0.22 \pm 0.59$	$-0.31 \pm 0.14 \pm 0.60$	$0.26 \pm 0.22 \pm 0.41$
10-20	$0.02 \pm 0.41 \pm 0.65$	$-0.53 \pm 0.30 \pm 1.58$	$-0.38 \pm 0.25 \pm 1.02$	$0.26 \pm 0.21 \pm 0.38$	$1.17 \pm 0.36 \pm 0.96$
20-30	$-0.37 \pm 0.37 \pm 0.95$	$-0.52 \pm 0.25 \pm 1.18$	$0.18 \pm 0.26 \pm 0.63$	$0.58 \pm 0.27 \pm 0.43$	$2.09 \pm 0.49 \pm 1.24$
30-40	$-0.43 \pm 0.36 \pm 1.46$	$0.30 \pm 0.25 \pm 0.48$	$0.36 \pm 0.25 \pm 1.07$	$-0.12 \pm 0.24 \pm 0.43$	$2.84 \pm 0.58 \pm 0.73$
40-50	$-0.47 \pm 0.29 \pm 1.22$	$-0.25 \pm 0.21 \pm 0.73$	$-0.46 \pm 0.22 \pm 0.83$	$0.55 \pm 0.26 \pm 0.52$	$3.13 \pm 0.61 \pm 0.66$
50-60	$-0.14 \pm 0.23 \pm 0.59$	$0.21 \pm 0.19 \pm 0.34$	$0.13 \pm 0.23 \pm 0.37$	$0.53 \pm 0.26 \pm 0.47$	$2.29 \pm 0.55 \pm 2.32$
60-70	$-0.24 \pm 0.17 \pm 0.42$	$0.03 \pm 0.15 \pm 0.26$	$-0.20 \pm 0.18 \pm 0.66$	$0.24 \pm 0.23 \pm 0.47$	$2.04 \pm 0.51 \pm 1.32$

TABLE V.  $dN_B/d\eta$  measured in Au+Au collisions at  $\sqrt{s_{NN}} = 19.6$  GeV. Uncertainties are  $1-\sigma$  statistical and 90% C.L. systematic. Yields are scaled up by a factor of 100 for clarity.

Centrality Bin (%)	Yield $\times 100$				
	$3.0 <  \eta  < 3.5$	$3.5 <  \eta  < 4.0$	$4.0 <  \eta  < 4.5$	$4.5 <  \eta  < 5.0$	$5.0 <  \eta  < 5.4$
0-10	$-0.09 \pm 0.41 \pm 1.15$	$-0.19 \pm 0.29 \pm 0.75$	$-0.04 \pm 0.23 \pm 0.84$	$-0.21 \pm 0.16 \pm 0.60$	$-0.29 \pm 0.10 \pm 0.63$
10-20	$0.17 \pm 0.40 \pm 0.80$	$0.70 \pm 0.35 \pm 1.04$	$0.41 \pm 0.28 \pm 1.03$	$0.06 \pm 0.18 \pm 0.43$	$0.32 \pm 0.29 \pm 0.37$
20-30	$-0.45 \pm 0.36 \pm 1.01$	$-0.45 \pm 0.24 \pm 1.34$	$-0.39 \pm 0.23 \pm 1.43$	$-0.23 \pm 0.22 \pm 0.43$	$1.60 \pm 0.46 \pm 0.94$
30-40	$0.38 \pm 0.40 \pm 0.95$	$0.17 \pm 0.26 \pm 0.76$	$0.16 \pm 0.25 \pm 1.01$	$0.01 \pm 0.24 \pm 0.54$	$2.31 \pm 0.56 \pm 1.03$
40-50	$0.45 \pm 0.31 \pm 0.95$	$0.05 \pm 0.22 \pm 0.82$	$-0.37 \pm 0.22 \pm 1.30$	$0.05 \pm 0.23 \pm 0.78$	$2.01 \pm 0.56 \pm 0.86$
50-60	$-0.11 \pm 0.22 \pm 0.89$	$0.07 \pm 0.18 \pm 0.50$	$-0.02 \pm 0.22 \pm 0.58$	$0.34 \pm 0.25 \pm 0.50$	$3.36 \pm 0.57 \pm 1.29$
60-70	$-0.29 \pm 0.15 \pm 0.75$	$-0.04 \pm 0.15 \pm 0.68$	$-0.11 \pm 0.18 \pm 0.47$	$0.03 \pm 0.21 \pm 0.38$	$1.71 \pm 0.48 \pm 0.46$

TABLE VI.  $dN_\alpha/d\eta$  measured in Cu+Cu collisions at  $\sqrt{s_{NN}} = 22.4$  GeV. Uncertainties are  $1\text{-}\sigma$  statistical and 90% C.L. systematic. Yields are scaled up by a factor of 10 for clarity.

Centrality Bin (%)	Yield $\times 10$				
	$3.0 <  \eta  < 3.5$	$3.5 <  \eta  < 4.0$	$4.0 <  \eta  < 4.5$	$4.5 <  \eta  < 5.0$	$5.0 <  \eta  < 5.4$
0-10	$-0.15 \pm 0.16 \pm 0.50$	$-0.16 \pm 0.09 \pm 0.56$	$0.28 \pm 0.04 \pm 0.50$	$0.87 \pm 0.07 \pm 0.50$	$1.94 \pm 0.07 \pm 0.50$
10-20	$0.21 \pm 0.08 \pm 0.50$	$0.21 \pm 0.14 \pm 0.50$	$0.63 \pm 0.06 \pm 0.50$	$2.04 \pm 0.09 \pm 0.50$	$5.06 \pm 0.09 \pm 0.79$
20-30	$0.11 \pm 0.09 \pm 0.50$	$0.20 \pm 0.08 \pm 0.50$	$0.77 \pm 0.06 \pm 0.50$	$2.62 \pm 0.10 \pm 0.55$	$7.35 \pm 0.12 \pm 1.34$
30-40	$0.08 \pm 0.08 \pm 0.50$	$0.09 \pm 0.07 \pm 0.50$	$0.75 \pm 0.06 \pm 0.50$	$2.80 \pm 0.07 \pm 0.50$	$8.09 \pm 0.12 \pm 1.37$
40-50	$0.13 \pm 0.10 \pm 0.50$	$0.11 \pm 0.06 \pm 0.50$	$0.66 \pm 0.05 \pm 0.50$	$2.47 \pm 0.06 \pm 0.50$	$7.23 \pm 0.11 \pm 1.19$
50-60	$0.08 \pm 0.05 \pm 0.50$	$0.12 \pm 0.06 \pm 0.50$	$0.45 \pm 0.04 \pm 0.50$	$1.95 \pm 0.05 \pm 0.50$	$5.99 \pm 0.10 \pm 1.04$

TABLE VII.  $dN_{Li}/d\eta$  measured in Cu+Cu collisions at  $\sqrt{s_{NN}} = 22.4$  GeV. Uncertainties are  $1\text{-}\sigma$  statistical and 90% C.L. systematic. Yields are scaled up by a factor of 100 for clarity.

Centrality Bin (%)	Yield $\times 100$				
	$3.0 <  \eta  < 3.5$	$3.5 <  \eta  < 4.0$	$4.0 <  \eta  < 4.5$	$4.5 <  \eta  < 5.0$	$5.0 <  \eta  < 5.4$
0-10	$0.61 \pm 0.40 \pm 2.40$	$0.41 \pm 0.37 \pm 0.71$	$0.25 \pm 0.09 \pm 0.53$	$0.37 \pm 0.08 \pm 0.40$	$0.03 \pm 0.12 \pm 0.42$
10-20	$0.05 \pm 0.22 \pm 2.15$	$0.12 \pm 0.22 \pm 0.58$	$0.39 \pm 0.10 \pm 0.80$	$0.46 \pm 0.10 \pm 0.54$	$0.40 \pm 0.17 \pm 0.40$
20-30	$0.45 \pm 0.18 \pm 1.03$	$0.14 \pm 0.20 \pm 0.77$	$0.19 \pm 0.09 \pm 0.61$	$0.13 \pm 0.12 \pm 0.58$	$0.96 \pm 0.23 \pm 0.49$
30-40	$0.44 \pm 0.18 \pm 1.25$	$0.28 \pm 0.18 \pm 0.68$	$0.24 \pm 0.09 \pm 0.40$	$0.19 \pm 0.08 \pm 0.66$	$1.23 \pm 0.31 \pm 0.68$
40-50	$0.28 \pm 0.11 \pm 0.80$	$0.26 \pm 0.15 \pm 0.41$	$0.14 \pm 0.07 \pm 0.40$	$0.17 \pm 0.08 \pm 0.40$	$1.22 \pm 0.22 \pm 0.40$
50-60	$0.20 \pm 0.10 \pm 0.65$	$0.20 \pm 0.10 \pm 0.40$	$0.03 \pm 0.07 \pm 0.40$	$0.10 \pm 0.07 \pm 0.40$	$0.90 \pm 0.24 \pm 0.41$

- 769 Rev. **C40**, 66 (1989). 793
- 770 [3] G. Singh and P. L. Jain, Z. Phys. **A348**, 99 (1994). 794
- 771 [4] M. L. Cherry *et al.* (KLMM Collaboration), Phys. Rev. 795
- 772 **C52**, 2652 (1995). 796
- 773 [5] A. Schuettauf *et al.* (ALADIN Collaboration), Nucl. 797
- 774 Phys. **A607**, 457 (1996). 798
- 775 [6] M. L. Cherry *et al.* (KLMM Collaboration), Z. Phys. 799
- 776 **C73**, 449 (1997). 800
- 777 [7] M. L. Cherry *et al.* (KLM Collaboration), Acta Phys. 801
- 778 Pol. **B29**, 2155 (1998). 802
- 779 [8] J. Barrette *et al.* (E877 Collaboration), Phys. Rev. **C61**, 803
- 780 044906 (2000). 804
- 781 [9] A. Dabrowska, B. Wosiek, C. J. Waddington, Acta Phys. 805
- 782 Pol. **B31**, 725 (2000). 806
- 783 [10] B. B. Back *et al.* (PHOBOS Collaboration), Nucl. Inst. 807
- 784 Meth. **A499**, 603 (2003). 808
- 785 [11] C. Adler *et al.*, Nucl. Instr. Meth. **A470**, 488 (2001). 809
- 786 [12] R. Bindel *et al.*, Nucl. Instr. Meth. **A474**, 38 (2001). 810
- 787 [13] E. Garcia *et al.*, Nucl. Instr. Meth. **A570**, 536 (2007). 811
- 788 [14] B. B. Back *et al.*, (PHOBOS Collaboration), Phys. Rev. 812
- 789 **C70**, 021901 (2004). 813
- 790 [15] B. Alver, M. Baker, C. Loizides, P. Steinberg, 814
- 791 arXiv:0805.4411v1 and references therein.
- 792 [16] B. B. Back *et al.*, (PHOBOS Collaboration), Phys. Rev. Lett. **91**, 052303 (2003).
- [17] M. Gyulassy and X. N. Wang, Comput. Phys. Commun. **83**, 307 (1994). Version 1.35 is used.
- [18] GEANT 3.21, CERN Program Library, Geneva.
- [19] B. B. Back *et al.* (PHOBOS Collaboration), Phys. Rev. **C65**, 031901 (2002).
- [20] B. Alver *et al.*, (PHOBOS Collaboration), Phys. Rev. **C83**, 024913 (2011).
- [21] B. Alver *et al.* (PHOBOS Collaboration) Phys. Rev. Lett. **102** (2009) 142301.
- [22] B. B. Back *et al.* (PHOBOS Collaboration), Nucl. Phys. **A757**, 28 (2005).
- [23] J. Beringer *et al.* (Particle Data Group), Phys. Rev. **D86**, 010001 (2012), see section 43.5.
- [24] B. B. Back *et al.*, (PHOBOS Collaboration), Phys. Rev. **C72**, 031901(R) (2005).
- [25] B. B. Back *et al.*, (PHOBOS Collaboration), Phys. Rev. **C74**, 021901(R) (2006).
- [26] B. Alver *et al.*, (PHOBOS Collaboration), Phys. Rev. Lett. **102**, 142301 (2009).
- [27] B. Alver *et al.*, (PHOBOS Collaboration), Phys. Rev. Lett. **98**, 242302 (2007).